SOLUTION-PROCESSED/EVAPORATION-BASED LIGHT-EMITTING DIODES OF FACE-DOWN/EDGE-UP ORIENTED COLLOIDAL QUANTUM WELLS

A THESIS SUBMITTED TO
THE GRADUATE SCHOOL OF ENGINEERING AND SCIENCE
OF BILKENT UNIVERSITY
IN PARTIAL FULFILLMENT OF THE REQUIREMENTS FOR
THE DEGREE OF
MASTER OF SCIENCE
IN
MATERIALS SCIENCE AND NANOTECHNOLOGY

By
Iklim Bozkaya
August 2023

SOLUTION-PROCESSED/EVAPORATION-BASED LIGHT-EMITTING DIODES OF FACE DOWN/EDGE-UP ORIENTED COLLOIDAL QUANTUM WELLS

By Iklim Bozkaya

August 2023

We certify that we have read this thesis and that in our opinion it is fully adequate, in scope and in quality, as a thesis for degree of Master of Science.

Hilmi Volkan Demir (Advisor)

Won Mi Ahn

Evren Mutlugün

Approved for the Graduation School of Engineering and Science:

Orhan Arıkan

Director of the Graduate School

ABSTRACT

SOLUTION-PROCESSED/EVAPORATION-BASED LIGHT-EMITTING DIODES OF FACE-DOWN/EDGE-UP ORIENTED COLLOIDAL QUANTUM WELLS

Iklim Bozkaya

M.S. in Materials Science and Nanotechnology

Advisor: Hilmi Volkan Demir

August 2023

Colloidal quantum wells (CQWs) have emerged as a quasi-two-dimensional class of semiconductor nanocrystals with the critical structural properties of being both atomically flat and vertically ultrathin. In these CQWs with atomically accurate thickness control, their extremely strong and precise one-dimensional quantum confinement, defined by few nanometers in sub-nm precision, gives rise to well-controlled anisotropic emission. The emission characteristics are composed by the contributions of transition dipole moments (TDMs), which are by their nature highly anisotropic in CQWs. In-plane TDMs lying in the lateral plane and out-of-plane TDMs along the vertical direction, taken with respect to the plane of a CQW, contribute to the emission characteristics proportionally. These features of CQWs make them highly attractive for use in light-emitting diodes (LEDs). In this thesis, to this end, in LEDs constructed either using all-solution based processing or evaporation, we show face-down and edge-up oriented self-assemblies of CdSe/$Cd_{0.25}Zn_{0.75}S$ core/hot-injection shell (HIS) grown CQWs, along with their Fourier analyses using back focal plane (BFP) imaging. Results show that the out-of-plane TDM distribution for all-face-down oriented CQW film is suppressed 4.1 times, with its in-plane TDM distribution reaching 92%. Thanks to the strong contribution from the in-plane TDMs, the corresponding angularly resolved distribution of luminescence exhibits a highly directional intensity profile for the film of face-down CQWs placed lying on a substrate. Used as an electroluminescent layer, all-face-down oriented CQWs enable extraordinarily large external quantum efficiency (EQE) increased by almost 2 folds compared to that of randomly-oriented CQWs, with EQE reaching 18.1% in the case of face-down orientation, a record high level for solution-processed CQW LEDs. Moreover, in this thesis work, for the edge-up oriented self-assemblies of CQWs creating superstructures in chain, we investigated the distribution of TDMs and discovered length of the chain formation of such stacked CQWs plays an essential role. Extending CQW chains from 50 to 500 nm

in length, on average in the film, the out-of-plane TDMs in the long-chained edge-up CQWs placed standing on a substrate is increased 3.5 times in comparison to those of the short-chained edge-up CQWs. The contribution of out-of-plane TDMs in directional emission is also improved via inducing longer chains. In the light of the results of Fourier image analysis, being used as the electroluminescent layer of evaporated LEDs in inverted architecture, all-edge-up oriented CQWs enable 50% enhancement in luminance levels compared to that of randomly-oriented CQWs. Additionally, in comparison to the face-down oriented CQWs used as the electrically driven emissive layer in the same device structure of LEDs, the edge-up oriented CQWs exhibit 60% improvement in charge injection. Such strongly orientation-dependent behavior of CQW layered structures, as exploited in this thesis, encourages further systematic studies on their ensemble optical emission characteristics in both solution-processed and evaporation-based LEDs and promises great potential for LED and other optoelectronic device applications.

Keywords: Colloidal quantum wells (CQWs), nanoplatelets, colloidal LEDs, all-solution-processed LEDs, self-assembly, face-down, edge-up, orientation-controlled film, transition dipole moment, single assembled monolayer.

ÖZET

ÇÖZELTİ İŞLEMLİ/BUHARLAŞTIRMA TABANLI YÜZ AŞAĞI/KENAR YUKARI YÖNLENDİRİLMİŞ KOLOİDAL KUANTUM KUYULARI IŞIK YAYAN DİYOTLARI

İklim Bozkaya

Malzeme Bilimi ve Nanoteknoloji, Yüksek Lisans

Tez Danışmanı: Hilmi Volkan Demir

Ağustos 2023

Koloid kuantum kuyuları (KKK), atomik düzeyde düz ve dikey olarak ultra ince olmak gibi kritik yapısal özellikleriyle yarıiletken nanokristallerin nispi-iki-boyutlu bir sınıfı olarak ortaya çıkmıştır. Atomik seviyede hassas kalınlık kontrolüne sahip bu KKK'larda nanometre altı hassaslıkla birkaç nanometre olarak tanımlanmış aşırı güçlü ve hassas bir-boyutlu quantum sıkıştırma, iyi kontrol edilen anizotropik yayılmaya sebebiyet verir. Yayılım karakteristikleri, KKKlarda doğaları gereği yüksek derecede anizotropik olan geçiş dipol momentlerinin (GDM) katkıları tarafından oluşturulur.KKK'ların düzlemleri düşünülerek, düzlem-içi GDM'ler yatay düzlemde ve düzlem-dışı GDM'ler dikey yön boyunca, yayılım karakteristiklerine orantısal olarak katkıda bulunurlar.KKK'ların bu özellikleri, opnları ışık yayan diyotlarda (IYD) kullanmak için son derece çekici hale getirir. Bu tezde, bu amaçlai tamamen çözelti tabanlı işleme veya buharlaşma kullanılarak oluşturulan IYD'lerde, CdSe/$Cd_{0.25}Zn_{0.75}S$ çekirdek/sıcak-enjeksiyon kabuğu (SEK) büyütülmüş KKK'ların yüz-aşağı ve kenar-yukarı yönlendirilmiş öz-düzenlemelerini ve geri odak düzlemi (GOD) görüntüleme kullanarak Fourier analizlerini gösteriyoruz. Sonuçlar, tüm yüz-aşağı yönlendirilmiş KKK filmi için dikey yöndeki GDM dağılımının %4.1 oranında baskılandığını ve düzlem içi GDM dağılımının ise %92'ye ulaştığını göstermektedir. Düzlem içi GDM'lerin güçlü katkısı sayesinde, buna karşılık gelen açısal olarak çözümlenmiş ışıldama dağılımı, altta yatan bir alt taşa yerleştirilen yüz aşağı yönlendirilmiş KKK filmi için oldukça yönel bir yoğunluk profili sergiler. Tüm-yüz-aşağı yönlendirilmiş KKK'lar, elektrolüminesans tabakası olarak kullanıldığında, rastgele yönlendirilmiş KKK'lara kıyasla neredeyse 2 kat artan olağanüstü büyük bir harici kuantum verimliliği (HKV) sağlar ve HKV yüz-aşağı yönlendirilmiş KKK'larda %18.1'e ulaşır, çözelti işlemeli KKK IYD'ler için kaydedilmiş en yüksek seviyedir. Ayrıca, bu tez çalışmasında, zincir süper yapılar oluşturan kenar-yukarı yönlü KKK öz-dizilimleri için GDM'lerin dağılımını araştırdık ve böyle yığılımış KKK'ların

zincir uzunluklarının önemli bir rol oynadığını keşfettik. Filmden ortalama olarak 50 ila 500nm uzunluğuna kadar olan KKK zincirleri boyunca, bir alt taşa dik şekilde yerleştirilen uzun-zincirli kenar-yukarı KKK'ların dikey yöndeki GDM'leri, kısa zincirli kenar-yukarı KKK'ların GDM'lerine kıyasla 3.5 kat artırılmıştır. Dikey yöndeki GDM'lerin yönel yayılmadaki katkısı, daha uzun zincir uzunlukları tetiklenerek iyileştirilir. Fourier görüntü analizinin sonuçlarına göre, ters mimariye sahip buharlaştırılmış IYD'lerin elektrolüminesan tabakası olarak kullanıldığında, tüm-kenar-yukarı yönel KKK'lar rastgele yönel KKK'lara kıyasla parlaklık düzeylerinde %50 artış sağlar. Ayrıca, aynı IYD cihaz yapısında elektrikle sürülen emisyon katmanı olarak kullanılan yüz aşağı yönlendirilmiş KKK'lara kıyasla, kenar yukarı yönlendirilmiş KKK'larda yük enjeksiyonunda %60'lık bir iyileşme gözlenmektedir. Bu tezde kullanılan KKK katman yapılarının güçlü bir şekilde yönlendirmeye bağlı davranışı, hem çözelti işlemeli hem de buharlaşma tabanlı IYD'lerde toplu optik emisyon özellikleri üzerine daha fazla sistemli çalışmaların yapılmasını teşvik ediyor ve IYD ve diğer optoelektronik cihaz uygulamalarında büyük potansiyel vaat ediyor.

Anahtar sözcükler: Kolloidal kuantum kuyuları, Çözelti-temelli ışık yayan diyotlar, öz-yapılandırma, yüz-aşağı, kenar-yukarı, yönlendirme kontrollü film, geçiş dipol momenti, tek katmanlı filmler.

Acknowledgement

To begin, I would like to express my gratitude to Prof. Hilmi Volkan Demir for his valuable support and direction throughout my thesis research. My supervisor, a remarkable mentor and leader, imparted invaluable knowledge to me during the duration of my thesis studies.

I would like to acknowledge the technical and administrative staff of UNAM for providing and sustaining a great research environment where I was able to complete my scientific work in the most desirable way.

I would also like to thank all my group members from Demir Research Group for a friendly work environment and for their teamwork. My special thanks go to LED group, Dr.Betül Canımkurbey, Ahmet Tarık Işık and İlayda Özkan for all the help and cooperation they provided throughout the development of this project. I also thank Özgün Akyüz, Emre Ünal, Rabia Önen, Dr. Zeynep Dikmen, Rabia Önen, Dr. Tatiana Lastovina, Dr. Aysan Khaligh Vazirabadi, Dr. Zahra Adelpour, Dr. Mojtaba Sadeghi, Farzan Shabani, Rumon Miah, Tuğba Karahan, Taha Haddadi, and Mohsin Waris. I will always remember the time we spent together, in terms of both our studies and the entertaining activities.

Finally, my special gratitude goes to my husband. I am grateful for his help and support during my thesis studies.

Contents

1 INTRODUCTION 1

2 SCIENTIFIC BACKGROUND 3

2.1. Colloidal Semiconductor Nanocrystals 3

2.1.1. Colloidal Quantum Wells (CQWs) 5

2.2. Nanocrystal Self-Assembly 7

2.2.1. Liquid-Interface Self-Assembly of Colloidal Quantum Wells 11

2.2.2. Electric Dipole Radiation of Colloidal Quantum Wells 14

2.3. LIGHT-EMITTING DIODES (LEDs) 19

2.3.1. LEDs Operating Principles 19

2.3.2. LED Architecture 20

2.3.3. Characterization of LEDs 23

3 EXPERIMENTAL METHODS 25

3.1. Synthesis of Materials 25

3.1.1. Cadmium Myristate 25

3.1.2. 4.5 ML CdSe Core CQWs 26

3.1.3. CdSe/CdZnS Core/Hot-Injection Shell (HIS) CQWs 26

3.1.4. ZnO and ZnMgO Nanoparticles 26

3.2. Self-Assembly of CQWs for their Face-Down and Edge-Up Orientation 27

3.3. LED Device Fabrication 31

3.4. LEDs Characterization 33

4 RESULTS AND DISCUSSION 36

4.1. All-Face-Down Oriented Colloidal Quantum Well Based Light-Emitting Diodes 36

4.2. All-Edge-Up Oriented Colloidal Quantum Well Based Light-Emitting Diodes 44

4.2.1. Control Mechanism of Edge-up Orientation Self-assembly of CQWs 44

4.2.2. Long-Chained and Short-Chained Edge-Up Oriented Colloidal Quantum Well Based Light-Emitting Diodes 49

4.3. Summary 53

5 Conclusion and Future Outlook 55

List of Figures

Figure 2. 1 Schematic diagram of energy band diagrams of bulk and nanocrystal structures with decreasing size. 3
Figure 2. 2 Energy-momentum diagram for direct bandgap semiconductors. 4
Figure 2. 3 Sketch of semiconductor nanocrystals with different dimensions of QDs (a), nanorods (b), and CQWs (c). 4
Figure 2. 4 High-angle annular dark-field transmission electron microscopy (HAADF-TEM) images of the 4.5 ML thick CdSe NPLs (a) [22], emission (dash line) and optical density (solid line) spectra of different monolayers of nanoplatelets (b) [21]. 5
Figure 2. 5 Schematic diagram of the heterostructures of CQWs as type-I (a), type-II (b), and quasi-type-II (c). 6
Figure 2. 6 Schematics of heterostructures of CQWs of core, core-crown, core/shell, and core-crown@shell. 7
Figure 2. 7 Electrostatic and steric stabilization of nanoparticles [26]. 7
Figure 2. 8 Energy diagram of interaction potential (U) as a function of the separation distance r between nanocrystals from dispersed to close-packed states (from the darkest to lightest solid lines) [25]. 8
Figure 2. 9 Absorbance spectrum, TEM image, and Grazing-Incidence Small-Angle X-ray Scattering (GISAXS) pattern of PbSe nanoparticles (a), micrograph of monolayer self-assembled of gold nanocrystals by drop-casting method, and the upper left inset shows interaction between neighbor Au nanocrystals, schematically, and the lower right inset shows Fourier transform image (b), schematic diagram of drop-casting approach in self-assembly (c) [28,29]. 9
Figure 2. 10 Schematic of self-assembly and transfer process onto a substrate adapted from ref. [30] (upper), and TEM images of self-assembled films (below) (a), schematic diagram of Langmuir-Blodgett method, and transfer to substrate based on the degree of holding a substrate, SEM images of self-assembled films [31,32] (b). 10
Figure 2. 11 TEM images of 3.1 and 8.0 nm PbS nanocrystals in organized films by the method of destabilization-based self-assembly, adapted with permission from Ref. [33] (a), the TEM images of assembled film of magnetic nanocrystals adapted with permission from Ref. [34] (b). 11
Figure 2. 12 TEM images of ellipsoidal and rhombic nanoplatelets of different types of crystalline superlattices obtained with liquid interfacial assembly technique, and the top insets show high-magnification TEM images, and the bottom insets show their small-angle electron diffraction patterns. Adapted with permission from ref. [35]. 12
Figure 2. 13 Schematic diagram of face-down and edge-up configuration self-assembly process for CdSe nanoplatelets (left panel), and TEM images of the face-down (a) and edge-up (b) configurations of CdSe self-assembled film [36]. 12
Figure 2. 14 Schematic diagram of liquid-interface self-assembly process (a), photo taken during the process (b), schematic diagram and SEM images of face-down and edge-up configurations of 4.5 ML CdSe (c,d) [37]. 13
Figure 2. 15 Illustration of three-layer system of air, thin-film, and substrate. 15
Figure 2. 16 Calculated back focal plane emission patterns of totally in-plane (a) and out-of-plane (b) transition dipole moments [41]. 17
Figure 2. 17 Back focal plane emission of a monolayer oriented of nanoplatelets and colloidal quantum dots (a), radiation intensity pattern of nanoplatelets and quantum dots as shown in blue and orange colors, respectively (b), and calculated spectra of pure IP, OP, and isotropic distribution of IP and OP (c) [42]. 17
Figure 2. 18 Experimental (a) and calculated pure in-plane transition dipole moment (b) back focal plane images of face-down oriented CdSe nanoplatelets, and their comparisons on dashed line fitting spectra (c). Experimental back focal plane images of edge-up oriented CdSe nanoplatelets (d), calculated 50% in-plane and 50% out-of-plane transition dipole moments (e), and their comparisons on dashed line fitting spectra (f) [36]. 18
Figure 2. 19 Schematic diagram for the working principle of light-emitting diodes. The external circuit of light-emitting diodes (a), and the behavior of conduction, valance band, and electron/hole injection resulting in radiative recombination and photon emission in the forward bias (b). 19

Figure 2. 20 Schematic illustrations of the simplest LED structure (a) and the corresponding energy band diagram (b). 20
Figure 2. 21 Illustration of an advanced structure of LEDs. 21
Figure 2. 22 Schematics of the normal and inverted structures of LEDs [46]. 22
Figure 2. 23 EQE measurement method in which a large photodetector is placed on an LED (a), and a photodetector is mounted on a goniometer to measure the angular distribution of the emission from an LED (b), and a LED is placed in an integrating sphere (c) with a spectrometer to measure the spectral power information. 23
Figure 2. 24 Conventional CIE diagram [54]. 24
Figure 2. 25 J-V characteristics. 24

Figure 3. 1 Self-assembly process on liquid interface. Subphase is filled into Teflon well (a), on top of the subphase, CQWs solution is dropped (b), and subphase is removed by a syringe (c). 28
Figure 3. 2 Schematic diagram of effect of the evaporation rate of solvent on the orientation of self-assembled CQW film. 29
Figure 3. 3 SEM images of our self-assembled films of CdSe/CdZnS core /HIS CQWs on Si substrates. Here, the solvent of CQWs used is hexane, and the subphases are acetonitrile (a), diethylene glycol (b), and ethylene glycol (c). Note that for each sets, the concentration of CQWs solution is 20 mg/mL and the amount of droppings is 20 μL in each case. 29
Figure 3. 4 SEM images of our self-assembled films of CdSe/CdZnS core /HIS CQWs on Si substrates. Here, the solvent of CQWs used is hexane, and the subphases are acetonitrile, while the concentration of CQWs solution is varied: 10 mg/mL (a), 20 mg/mL (b), and 30 mg/mL (c). Note that for each set, the amount of dropping is 20 μL. 30
Figure 3. 5 Optimized all edge-up (a) and face-down (b) orientated self-assembled CQW films on Si substrate. 31
Figure 3. 6 ITO coated glass substrate used in this thesis work. 31
Figure 3. 7 Photograph of our BFP setup. 34
Figure 3. 8 Schematic diagram of our BFP setup and the trace of optical beams. 34

Figure 4. 1 TEM image of our hot-injection shell grown CQWs. The face-down and edge-up orientations of these CQWs co-exist in this image. 37
Figure 4. 2 Scanning electron microscopy (SEM) image of all-face-down oriented monolayer (a) and randomly-oriented spin-coated (b) CQW films with atomic force microscopy (AFM) measurements of them. Inset: Schematic diagrams of CQWs films with polarization of emission of self-assembled (a) and spin-coated (b). 38
Figure 4. 3 BFP image patterns of the calculated emission profile and intensity diagrams of 100% in-plane TDMs (a) and 100% out-of-plane TDMs (b). Measured BFP image patterns and fitted k-space-dependent intensity profiles on the p-pol orientation of the face-down oriented self-assembly (c) and the spin-coated CQWs films (d). Corresponding polar intensity diagrams (e) of the face-down oriented self-assembly (blue), and the spin-coated (orange) CQWs films. 39
Figure 4. 4 Schematic illustration of device structure (a), energy level diagram (b), and cross-section image of our CQW-LEDs with the face-down oriented monolayer CQWs via transmission electron microscopy (TEM) along with energy-dispersive X-ray spectroscopy (EDAX) mapping (c). 40
Figure 4. 5 TEM image of ZnMgO nanoparticles synthesized. 41
Figure 4. 6 Angular distribution of extracted light emission from LEDs with the emissive layer of the oriented and random CQWs, experimentally measured (a) and numerically calculated (b). 42
Figure 4. 7 Normalized electroluminescence (EL) intensity spectrum (a), and EQE versus current density (b) of the face-down oriented-CQW-LED and the random-oriented CQW-LED devices. Current density versus voltage of the random-oriented CQW-LED (c) and the face-down oriented-CQW-LED (d). 43
Figure 4. 8 SEM images of the self-assembled films of CdSe/CdZnS core/HIS CQWs on Si substrates. The solvent of CQWs is hexane, and the subphase is acetonitrile (a), diethylene glycol (b), and ethylene glycol (c).

Note that, for each set, the concentration of CQW solution is 15 mg/mL and the amount of dropping is 20 μL. 45
Figure 4. 9 SEM images of the self-assembled film of our CdSe/CdZnS core/HIS CQWs on Si substrates. The subphase is ethylene glycol, and the solvents are hexane (a), heptane (b), and octane (c). Note that, for each set, the concentration of CQWs solution is 15 mg/mL and the amount of dropping is 20 μL. 46
Figure 4. 10 SEM images of the edge-up self-assembled film of our CdSe/CdZnS core/HIS CQWs on Si. The subphase is ethylene glycol, and the solvent is octane with concentrations of 10 mg/mL (a), 20 mg/mL (b), and 30 mg/mL (c).....47
Figure 4. 11 SEM images of the edge-up self-assembled films of our CdSe/CdZnS core/HIS CQWs on Si. The subphase is ethylene glycol, and the solvent is octane with concentrations of 26 mg/mL for the long chain (a), 24 mg/mL for the middle chain (b), and 20 mg/mL for the short chain (c). 48
Figure 4. 12 Numerically calculated and experimentally measured BFP images, and the polar plots of a single particle (a), short-chained (b) and long-chained (c) edge-up oriented CQWs.....48
Figure 4. 13 Schematic illustration of the structure (a) and energy level diagram of LEDs (b) we fabricated. 50
Figure 4. 14 EL spectra of our LED with the spin-coated, face-down, and edge-up oriented CQW EML. Inset: photograph of the LED with edge-up oriented CQW EML driven at 7 V. …….. 51
Figure 4. 15 EQE vs. voltage, current density vs. voltage, and luminance level of LEDs using EMLs of the long-chained and short-chained edge-up oriented CQWs with the control groups of face-down oriented and spin-coated CQWs.....52
Figure 4. 16 Current density vs. voltage graph of the electron-only devices using different configurations of CQWs.....52
Figure 4. 17 Atomic force microscopy (AFM) results of the device layers used in the structure of our LEDs. 53

CHAPTER 1

1 INTRODUCTION

From universe to nanoscale entities, light is the main source to observe surroundings of humans, and we human beings have been constructing illumination sources to discover these since early 19th century [1]. Until today, continuous progress in artificial illumination sources has been demonstrated. During all of these efforts, a large variety of materials have been used including rare earth elements [2], organic dyes [3], and electroluminescent phosphors [4]. However, these efforts have suffered inefficiency, insufficient lifetime and/or unstable color control.

In the 20th century, semiconductors made it possible to obtain high-performance light-emitting devices thanks to their attractive properties such as direct bandgap transition, compact-size fabrication, low production costs, and precise color control. In the light of these advantages, semiconductors including quantum wells [5], quantum dots [6], and perovskites [7] have been used as emissive materials of light-emitting devices.

Semiconductor colloidal quantum wells, also known as nanoplatelets, have a quasi-two-dimensional structure with atomically controlled vertical thickness. Compared to other semiconductor nanocrystals, they offer unique optical properties such as narrow emission bandwidth, extremely large absorption cross-section, and anisotropic transition dipole moments thanks to their strong quantum confinement in the vertical direction. These properties make them promising for light-emitting diodes with high external quantum efficiency and brightness [8]. However, the aim for high efficiency from light-emitting diodes requires enhancement in light-extraction efficiency due to their otherwise limited level of outcoupling from higher refractive index medium to air.

Oriented self-assembly of the colloidal quantum wells is a technique of deposition thin-film which allows the control on their orientation. Self-assembly method offers the benefits of making uniform

and pinhole-free films with well-defined orientation control over large areas during the formation of thin-film [9]. The inherent direction-dependent emission properties of colloidal quantum wells [10], their face-down and edge-up orientated self-assembly, allows us to control directionality of the emission. In previous reports [11], such properties of colloidal quantum wells used as passive thin-films have been exploited under optical excitation. In this regard, self-assembled colloidal quantum wells are highly advantageous for improvement of light-extraction efficiency of light-emitting diodes. We target to use self-assembled colloidal quantum wells as the active emissive layer to overcome the light-extraction efficiency limitation. The control on transition dipole moments and directionally of emission enables the control on light intensity profile generated by light-emitting diodes.

In this thesis, we, first, demonstrated high-performance solution-processed colloidal quantum well based light-emitting diodes having all-face-down self-assembled monolayer film of colloidal quantum wells as the emissive layer. During this work, Fourier image analysis on face-down orientated self-assembled colloidal quantum well shows that majority of the contribution of the transition dipole moments (TDMs) comes from the in-plane TDMs with a ratio of 92%. Here, we optimized conventional light-emitting diode structure with all-face-down oriented colloidal quantum wells as the emissive layer with the device architecture consisting of consecutive layers of indium tin oxide (ITO, 100 nm)/poly(ethylene dioxythiophene):polystyrene sulphonate (PEDOT:PSS, 30 nm)/poly (N,N9-bis(4-butyl phenyl)-N,N9 bis(phenyl)-benzidine) (p-TPD, 20 nm)/poly(9-vinyl carbazole) (PVK, 10 nm)/colloidal quantum well/ $Zn_{0.95}Mg_{0.05}O$ (30 nm)/Al(100 nm). In regard of this structure of light-emitting diodes, the outcoupling efficiency reaches 34%, which is higher than 22% of the conventional light-emitting diodes with randomly-oriented colloidal quantum wells. Our all-face-down monolayer self-assembled colloidal quantum well based light-emitting diodes achieve a record high level of external quantum efficiency of 18.1% with a high luminance level of 19,800 cd/m^2.

Second, we proposed optimizations of all-edge-up orientated self-assembled colloidal quantum well films with the control on the length of their chains of edge-up stacks. Revealed by the Fourier image analysis of short and long-chain edge-up oriented colloidal quantum wells, the contribution of out-of-plane transition dipole moments increases 3.5 times. We showed inverted-structure light-emitting diodes with all-edge-up oriented colloidal quantum well as the emissive layer with the device architecture made of indium tin oxide (ITO, 100 nm)/ZnO (40 nm)/colloidal quantum well/ 4,4′-Bis(N-carbazolyl)-1,1′-biphenyl (CBP, 60 nm)/ molybdenum oxide (MoO_3, 8 nm)/Al (100 nm). In regard of this structure of the light-emitting diodes, the improvement of charge injection is 60% for both short- and long-chain edge-up oriented colloidal quantum wells with respect to the face-down oriented colloidal quantum wells. At the same time, comparing the long-chained edge-up oriented films to the short-chained ones, more than 50% enhancement is observed with including long-chain.

CHAPTER 2

2 SCIENTIFIC BACKGROUND

2.1. Colloidal Semiconductor Nanocrystals

Colloidal nanocrystals (NCs) are composed of inorganic semiconductor materials of which size is measured in nanometers. The first reproducible colloidal synthesis of NCs was reported in 1993 by Murray *et al.* [12]. NCs exhibit size-dependent physical properties, which is explained by the quantum confinement effect [13]. When the size of a NC is comparable to the Bohr radius exciton, one may assume finite barrier potential confining the electron-hole pair. This effect was firstly observed in 1980s by Ekimov *et al.* [14]. Shrinking the size of NCs leads to the separation of energy levels. Therefore, the energy band gap between the highest unoccupied (conduction band) and lowest occupied (valence band) molecular energy level separates further and energy bands are discretized more [15] as schematically shown in Figure 2.1.

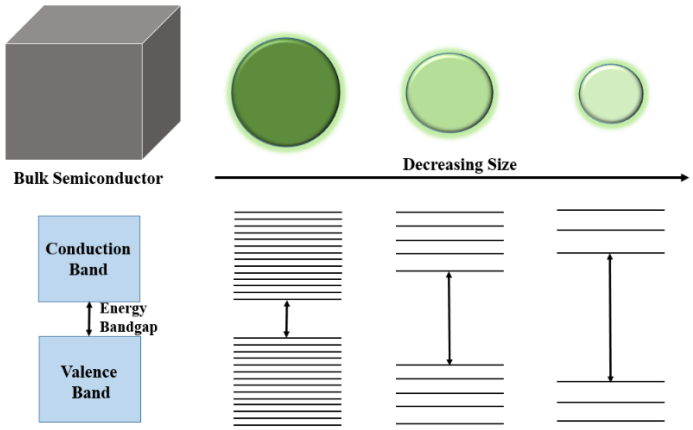

Figure 2. 1 Schematic diagram of energy band diagrams of bulk and nanocrystal structures with decreasing size.

The quantum confinement directly affects optical properties of NCs such as optical absorption and emission spectra. This model gives perturbation energy due to confinement effect such that [16]

$$\Delta E \approx \frac{\hbar^2 \pi^2}{2\mu R^2} \text{ and } \frac{1}{\mu} = \frac{1}{m_e^*} + \frac{1}{m_h^*} \quad (1)$$

where ħ is the reduced Planck's constant, R is radius of NCs, μ is reduced exciton mass, m_e and m_h are the effective masses of electron and hole. The emission and absorption of NCs are set by discretized energy levels and energy bandgap of NCs as well as, their effective electron and hole masses according to (1), and the energy level diagram is shown in Figure 2.2.

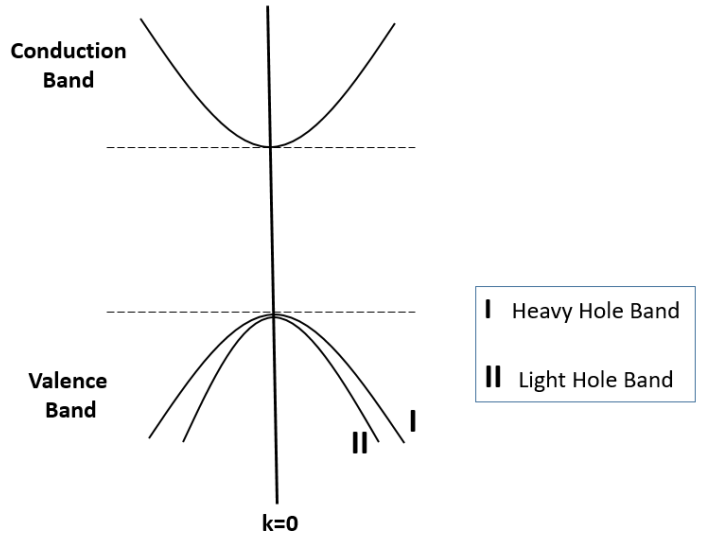

Figure 2. 2 Energy-momentum diagram for direct bandgap semiconductors.

Semiconductor colloidal NCs, that we use, have elemental composition of II-VI groups of elements, and may have the dimensions of quasi-zero-dimension (quasi-0D), one-dimensional (1D), and two-dimensional (2D), known as colloidal quantum dots (CQDs) [17], nanorods [18], and colloidal quantum wells (CQWs) [19], respectively (see Figure 2.3). The dimensions of the confinement effect of QDs, nanorods, and CQWs are, also in three, two, and one dimension, respectively.

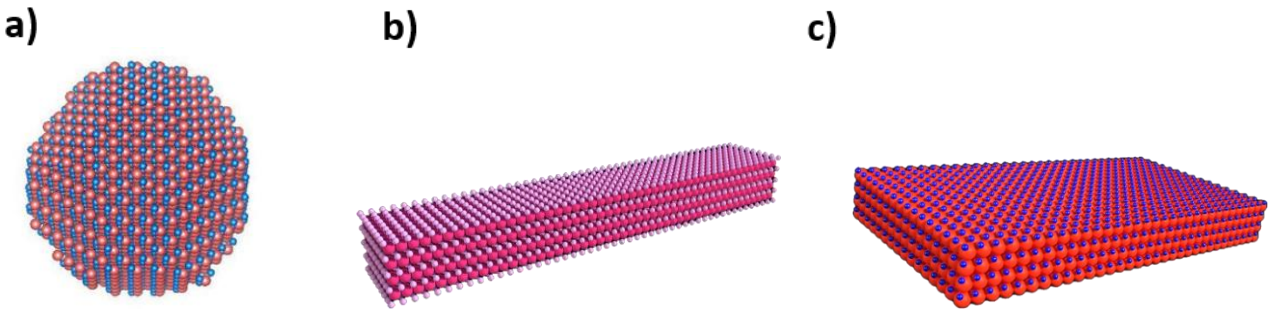

Figure 2. 3 Sketch of semiconductor nanocrystals with different dimensions of QDs (a), nanorods (b), and CQWs (c).

2.1.1. Colloidal Quantum Wells (CQWs)

CQWs are quasi-2D NCs whose lateral size is in tens of nanometers while their vertical thickness is only few nanometers, relatable to their exciton Bohr radius. This shape causes one-dimensional quantum confinement perpendicular to the lateral surface to reduce inhomogeneous broadening related to the lateral size dispersion. Therefore, the features of narrow emission bandwidth of CQWs positively distinguishes from other NCs. The report of Ithurria *et al.* is the first report of reproducible colloidal synthesis of CdSe quantum wells in 2011 [20]. This work demonstrated zinc-blende CdSe CQWs with different thickness of 3.5, 4.5, and 5.5 monolayers (MLs). The emission and photoluminescence spectra of 3.5, 4.5 and 5.5 ML CdSe CQWs [21] and TEM image of 4.5 ML CdSe CQWs [22] are shown in Figure 2.4.

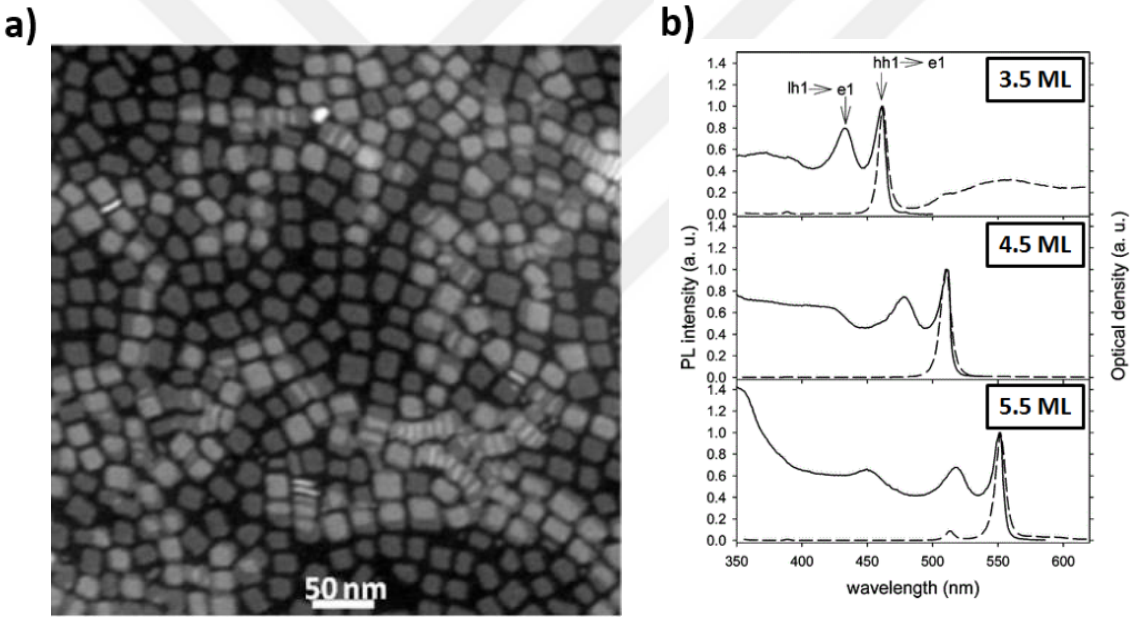

Figure 2. 4 High-angle annular dark-field transmission electron microscopy (HAADF-TEM) images of the 4.5 ML thick CdSe NPLs (a) [22], emission (dash line) and optical density (solid line) spectra of different monolayers of nanoplatelets (b) [21].

As shown in Figure 2.4, the electron-heavy hole peak is at around 460, 512, and 550 nm for 3.5, 4.5, and 5.5 ML CdSe CQWs, respectively, since as mentioned before, the energy levels vary with different thicknesses in agreement with the quantum confinement effect. CQWs feature emission and absorption spectrum overlap with very small Stokes shifts of around 2 nm and homogeneous broadening in their emission spectrum. Additionally, the full-width-at-half-maximum (FWHM) of their emission is as narrow as 35 meV at room temperature [21].

Unlike CQDs of which spectral tuning is continuously adjusted by varying their radius, adding monolayers to CQWs induces discrete tuning spectral peaks with shifts in the range of 100 meV due to the quantum confinement. On the other hand, engineering of the heterostructures of CQWs is alternative for continuous emission wavelength shifting in CQWs.

Heterostructures of CQWs, such as core-shell, provide different electron-hole localization regimes as an additional degree of freedom, improving targeted optoelectronic properties. There are three types of heterostructures of CQWs: type-I, type-II and quasi type-II (see Figure 2.5) [22,23]. Type-I structure includes narrow bandgap materials as the core, and the core is covered by wide bandgap materials for passivation of surface states and electron-hole confinement in the core leads to direct exciton formation. This can be implemented completely in an "inverted" structure where both electron and hole are confined in the same region outside the core. For type-II structure, asymmetrical bandgap materials are used to obtain the separation of electron-hole wavefunctions in different parts. On the other hand, in quasi type-II structure one of the wavefunction is confined while the other is delocalized, which is typically the electron due to its lighter mass.

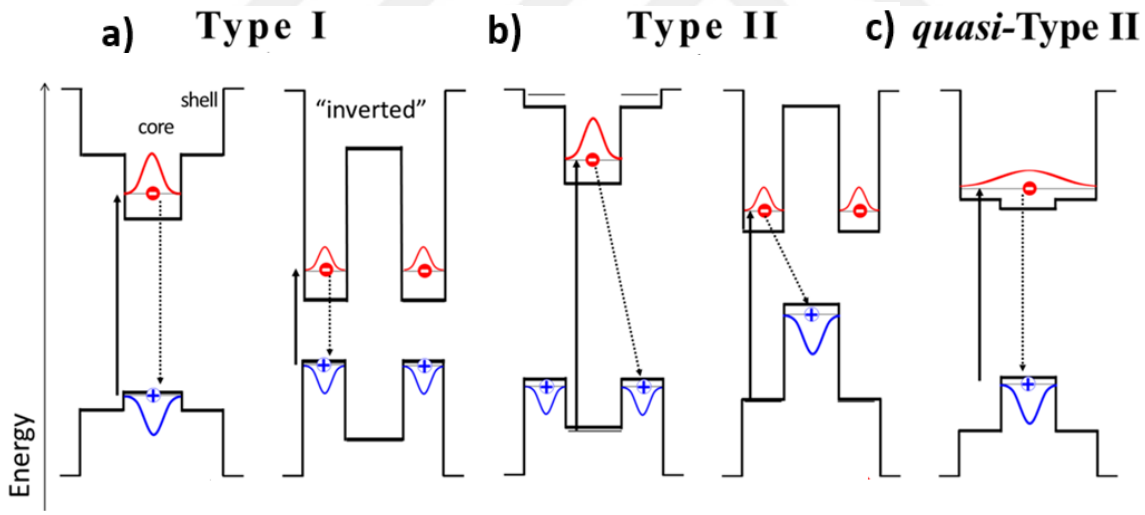

Figure 2. 5 Schematic diagram of the heterostructures of CQWs as type-I (a), type-II (b), and quasi-type-II (c).

Heterostructures of CQWs can be formed with core-shell, core-crown, and a more complicated structure of core-crown@shell with different material and types as shown in Figure 2.6 [24].

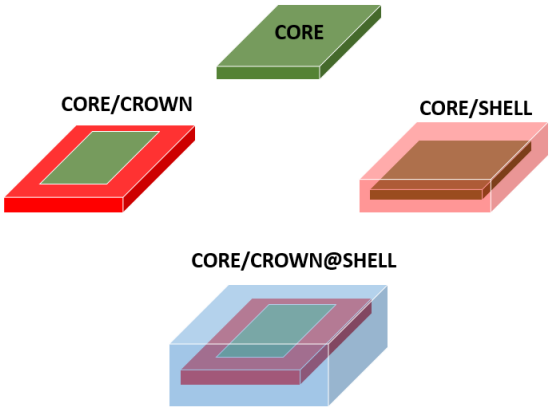

Figure 2. 6 Schematics of heterostructures of CQWs of core, core-crown, core/shell, and core-crown@shell.

2.2. Nanocrystal Self-Assembly

Self-assembly is a spontaneous process that transforms atoms, molecules, and nanoparticles into organized structures from their mobile states in which pair potential is dominantly repulsive. In this system, connection of molecular chains and nanocrystal surface may provide steric stabilization while adsorption of charges may allow for electrostatic stabilization of nanocrystals (see Figure 2.7). This allows for dispersion of nanocrystals in polar and nonpolar solvents [25].

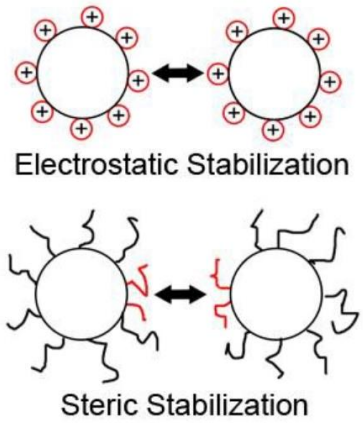

Figure 2. 7 Electrostatic and steric stabilization of nanoparticles [26].

Ordered organization of nanocrystals needs attractive forces, and this can be induced by the processes of removal of solvents, cooling the solution, and cross-linking of capping ligands [25]. During the self-assembly processes, repulsive forces originating from steric or electrostatic stabilization must change to attractive forces. Completely removal of solvent composes assembled of NCs with interparticle separation set by the balance between the ligand repulsion forces and van der Walls attraction forces [27]. As a result, the potential of self-assembled NCs is lower than the characteristic thermal energy, k_BT of systems as can be seen in Figure 2.8 [25].

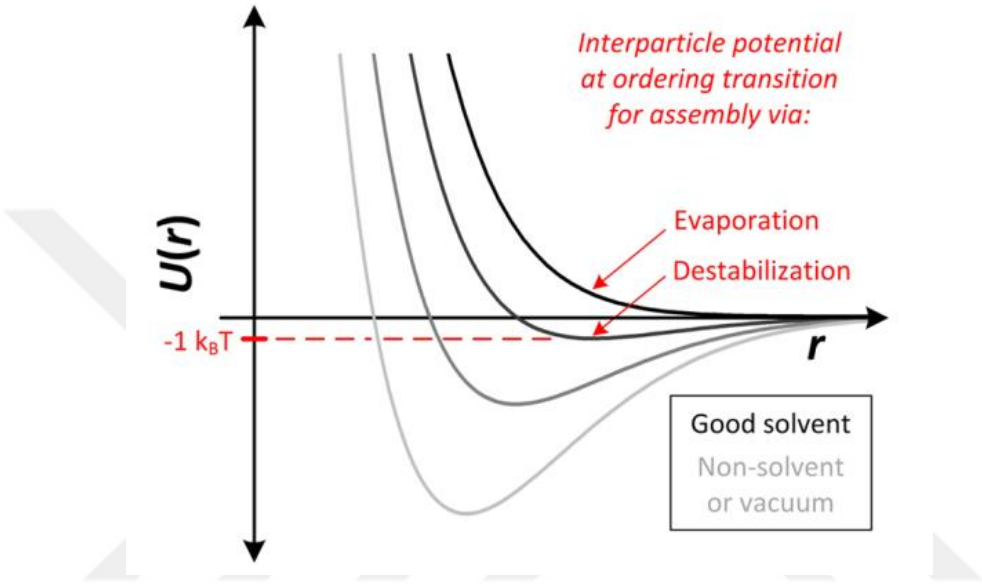

Figure 2. 8 Energy diagram of interaction potential (U) as a function of the separation distance r between nanocrystals from dispersed to close-packed states (from the darkest to lightest solid lines) [25].

Evaporation and destabilization of NCs solution are two methods used to prepare self-assembled NCs. Evaporation-based self-assembly is used for superlattice thin-films formed during drying process of solvent. There are few approaches relying on evaporation method. Drop-casting is based on small amount of dilute NC solution dropped on solid subphase and subsequent evaporation of the solvent of NCs. Mixing of solvents of hexane and octane to reach long-chain superstructures via drop-casting reported by Talapin *et al.* in 2005 (see Figure 2.9a) [28]. The same method also used by Bigioni *et al.* for a gentle deposition of Au nanocrystal solution showed Au self-assembled film on air-liquid interface (see Figure 2.9b, c) [29].

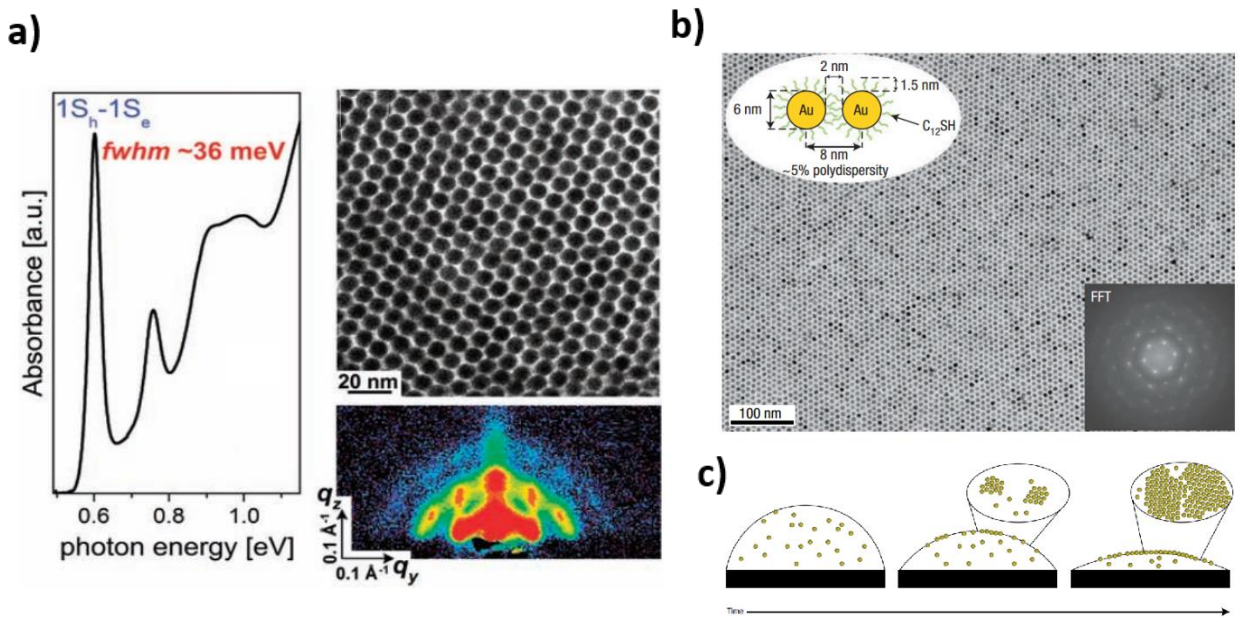

Figure 2. 9 Absorbance spectrum, TEM image, and Grazing-Incidence Small-Angle X-ray Scattering (GISAXS) pattern of PbSe nanoparticles (a), micrograph of monolayer self-assembled of gold nanocrystals by drop-casting method, and the upper left inset shows interaction between neighbor Au nanocrystals, schematically, and the lower right inset shows Fourier transform image (b), schematic diagram of drop-casting approach in self-assembly (c) [28,29].

A polar liquid, diethylene glycol, was used to form NC superlattices, from their dispersion in nonpolar solvent. Large-scale membranes of long-range ordered nanocrystals at liquid-air interface can be induced and transferred onto a solid substrate (see Figure 2.10a) [30]. Langmuir−Blodgett method, also contains this approach enforcing lateral surface pressure to obtain a monolayer of self-assembled film to sink onto a solid substrate (see Figure 2.10b) [31,32].

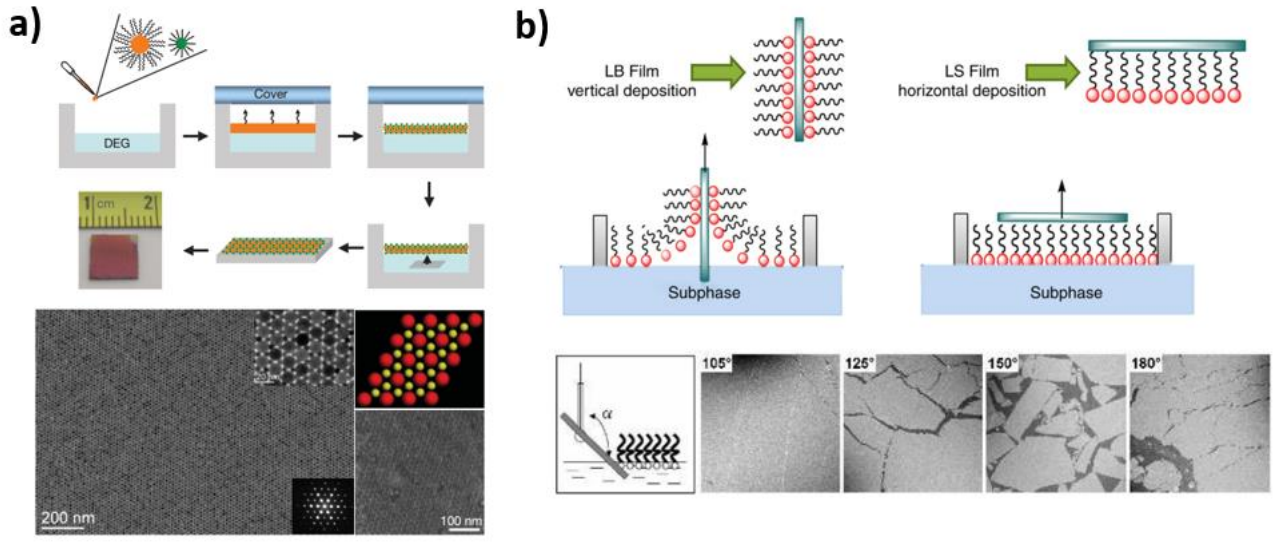

Figure 2. 10 Schematic of self-assembly and transfer process onto a substrate adapted from ref. [30] (upper), and TEM images of self-assembled films (below) (a), schematic diagram of Langmuir-Blodgett method, and transfer to substrate based on the degree of holding a substrate, SEM images of self-assembled films [31,32] (b).

Destabilization-based self-assembly relies on two forces in which attractive forces between NCs are more favorable than the repulsive forces of ligands between them when the capping layers of NCs is mixing in solvent. The polarity of NC solution can be increased by controlled diffusion of nonsolvent to stimulate flocculation when placing a layer of nonsolvent above NC solution in a test tube, induced precipitation of NCs at the bottom of a tube without intermixing of liquids. This approach produces closed-pack assembles instead of thin-film. In the report of Rupic *et al.*, the colloidal solution of 3.1 and 8.0 nm size PbS nanocrystals is toluene, and ethanol is used as a nonsolvent to form superlattice on silicon substrate, as shown in Figure 2.11a [33].

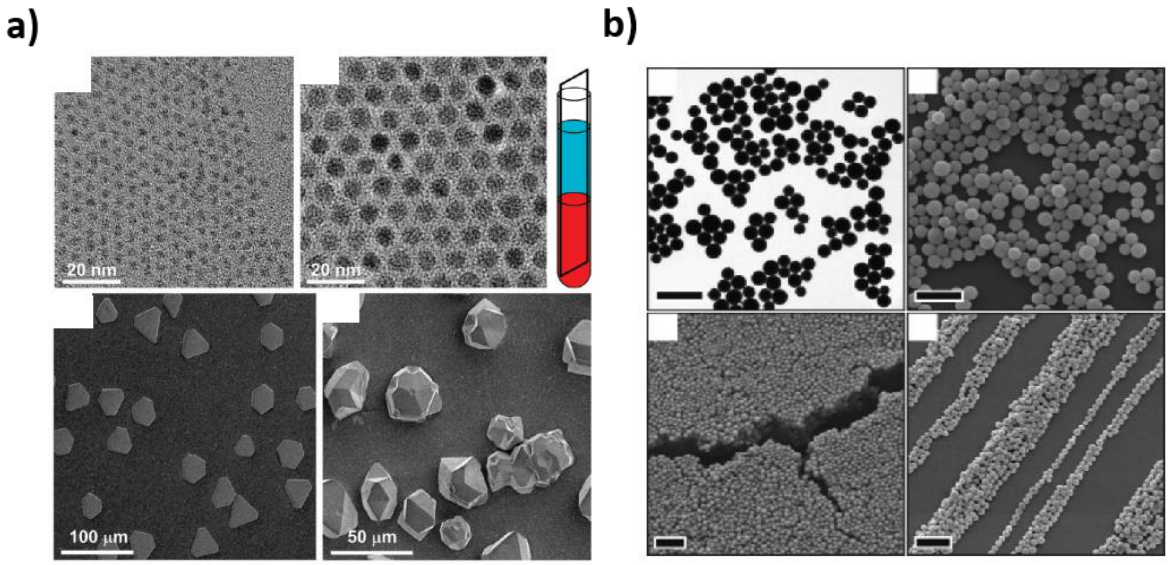

Figure 2. 11 TEM images of 3.1 and 8.0 nm PbS nanocrystals in organized films by the method of destabilization-based self-assembly, reprinted (adapted) with permission from [33]. Copyright {2010} American Chemical Society. (a), the TEM images of assembled film of magnetic nanocrystals, reprinted (adapted) with permission from [34]. Copyright {2007} American Chemical Society. (b).

Another method of the destabilization-based self-assembly is induced from the interaction between polar and nonpolar solvents by distributing the surfactant bilayer. In this line, hydrophilic ligands of NCs with dodecyltrimethylammonium bromide (DTAB) provides the formation of a superlattice resulting from attractive van der Waals forces (see Figure 2.11b) [34]. Self-assembly of NCs with two methods of evaporation and destabilization of nanocrystal solutions is affected by different parameters such that the quality of solvent of NCs, temperature of solutions and environment, and chosen solid substrates and liquid.

2.2.1. Liquid-Interface Self-Assembly of Colloidal Quantum Wells

The early report of Paik *et al.* in 2011 focuses on uniform liquid-interface self-assembly of platelet-shaped nanocrystals [35]. In this study, derivatives of ethylene glycol were used as liquid subphase for the deposition of GdF_3, and the results show that increment of the polarity of subphase induces tendency to orient nanoparticles. In this regard, while the most polar subphase ensures edge-up oriented self-assembly of GdF_3 nanoplatelets, the least polar one causes face-down oriented assembly (see Figure 2.12).

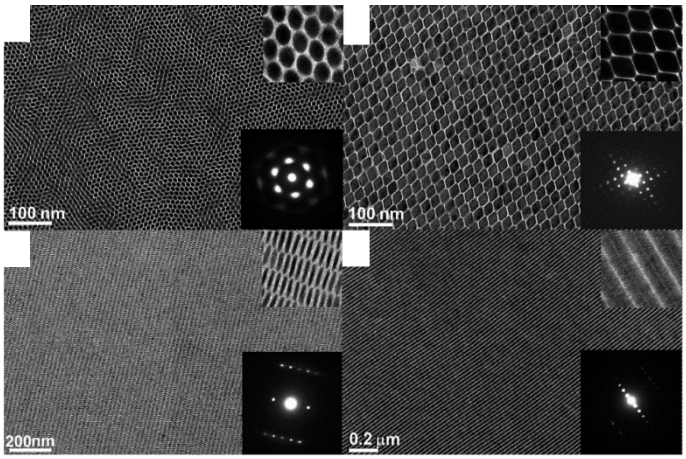

Figure 2. 12 TEM images of ellipsoidal and rhombic nanoplatelets of different types of crystalline superlattices obtained with liquid interfacial assembly technique, and the top insets show high-magnification TEM images, and the bottom insets show their small-angle electron diffraction patterns. Reprinted (adapted) with permission from [35]. Copyright {2007} American Chemical Society.

Using a similar methodology, Gao *et al.* in 2017 showed the orientation-controlled self-assembly of 5.5 ML CdSe core nanoplatelets by tuning interactions between the surface ligands of NPLs and the liquid subphase when adding oleic acid into diethylene glycol as a surfactant is used as the liquid subphase [36]. Herein, this previous work reported that a concentration of oleic acid higher than 4.2 mM resulted in face-down oriented self-assembly while a concentration of oleic acid lower than 0.42 mM causes edge-up oriented self-assembly of CdSe NPLs (see Figure 2.13).

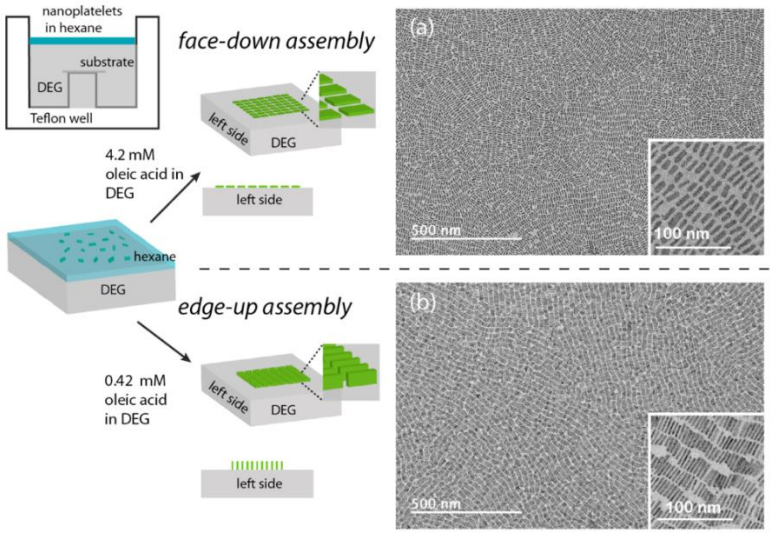

Figure 2. 13 Schematic diagram of face-down and edge-up configuration self-assembly process for CdSe nanoplatelets (left panel), and TEM images of the face-down (a) and edge-up (b) configurations of CdSe self-assembled film [36].

In the work of Erdem *et al.*, liquid-interface self-assembly of 4.5 ML CdSe colloidal quantum wells transferred into silicon substrate was reported with high surface coverage on a large scale [37]. Here, the solvent of NPLs was hexane, and the liquid subphases used were acetonitrile (ACN) and ethylene glycol (EG) (see Figure 2.14).

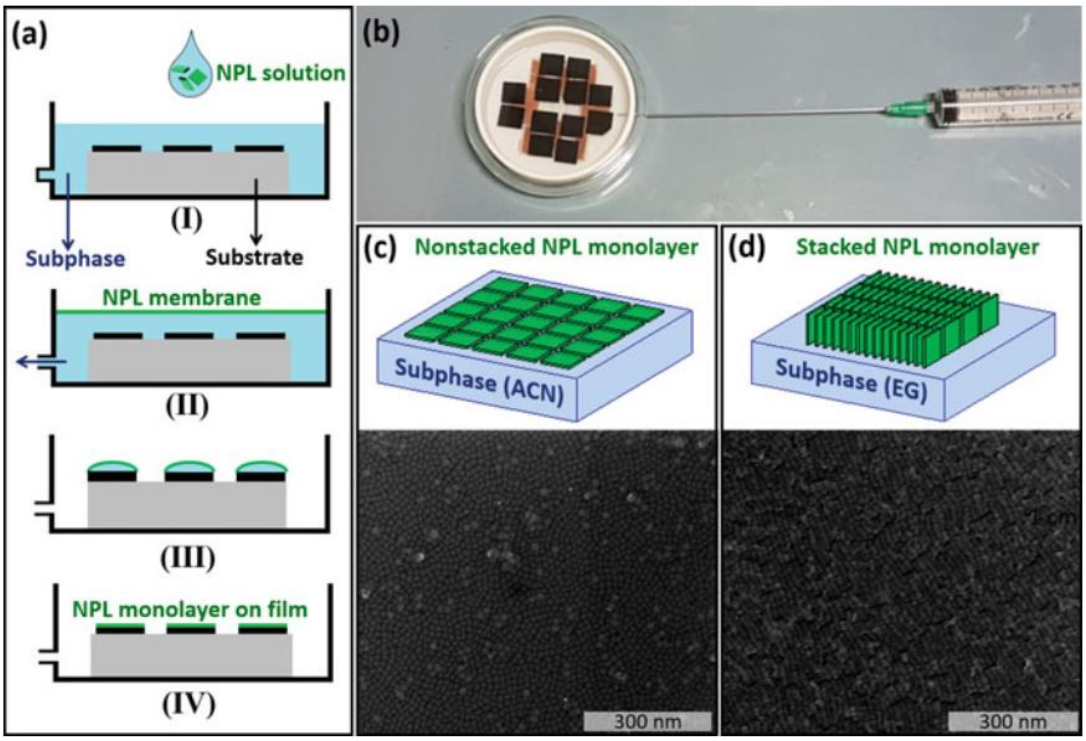

Figure 2. 14 Schematic diagram of liquid-interface self-assembly process (a), photo taken during the process (b), schematic diagram and SEM images of face-down and edge-up configurations of 4.5 ML CdSe (c,d) [37].

For the nonstacked (face-down self-assembly) NPL monolayer, the ACN was used, while stacked (edge-up self-assembly) NPL monolayer was obtained using the EG as subphase. Moreover, the used amount of dropping and the used concentration of NPL solution were critical to obtaining different orientations such that 2.1×10^{-7} M and 4.3×10^{-7} M of 60 µL NPL solution was dropped on the subphase for deposition of nonstacked and stacked NPL monolayer on substrate, respectively. In Table 2.1, a list of some recent reports of the liquid-interface self-assembly of nanoplatelets is given.

Table 2.1 The previous reports of the liquid-interface self-assembly of different nanoplatelets and the resulted orientations when kinds of solvents, ligands and subphases are used.

Report	Nanoplatelets	Solvent	Ligand	Subphase	Orientation
[35]	GdF_3	hexane	oleic acid	ethylene glycol	edge-up
				diethylene glycol	mixed
				3-ethylene glycol	face-down
				4-ethylene glycol	face-down
[37]	4.5 ML CdSe	hexane	oleic acid	acetonitrile	face-down
				ethylene glycol	edge-up
[38]	4.5 ML CdSe	hexane	myristic acid	acetonitrile	face-down
				acetonitrile	edge-up
[39]	CdSe/CdZnS core/shell	hexane	oleic acid and oleylamine	diethylene glycol	face-down

Orientation-controlled self-assembly of colloidal quantum wells enable to control anisotropic effect on the emission characteristic of NPLs by transition dipole moments, leading to directional emission properties of NPLs. This advantages can be exploited in applications including light-emitting diodes.

2.2.2. Electric Dipole Radiation of Colloidal Quantum Wells

The emission from nanocrystals originates from the transition dipole moment, and the radiation pattern coming from the electric dipole emitters varies in homogeneous and inhomogeneous optical environment.

Within homogeneous isotropic medium, the emission rate is defined by the Einstein A coefficients given by Fermi's golden rule [40,41] such that

$$A_{ED}(\omega) = \rho_0(\omega)\frac{\pi\omega}{3\hbar}\frac{|\mu_{ED}(\omega)|^2}{\varepsilon} \quad (2)$$

where $\varepsilon = \varepsilon_r\varepsilon_0$ is the absolute permittivity and $\mu = \mu_r\mu_0$ is the absolute permeability which defines homogeneous medium, ω is the emission frequency, $\rho_0(w) = {w^2(\varepsilon\mu)^{3/2}}/{\pi^2}$ is the density of electromagnetic states, and μ_{ED} is the electric transition dipole moment.

As mentioned, in nonhomogeneous medium, the local density of electromagnetic states is changed. The emission rate in terms of frequency, polarization of transverse-electric (TE, s) and transverse-magnetic (TM, p), and in-plane momentum ($\boldsymbol{k}_{II}$) is described as

$$\Gamma_{ED}^{s,p}(\omega, \boldsymbol{k}_{II}) = A_{ED}(w)\tilde{\rho}_{ED}^{s,p}(\omega, \boldsymbol{k_{II}}) \tag{3}$$

where $\tilde{\rho}_{ED}^{s,p}$ is the normalized electric local density of optical states. For isotropic transition dipole moments, the resulted emission rate is [41]

$$\Gamma_{ED}^{s,p}(\omega, \boldsymbol{k}_{II}) = \left(\frac{|\mu_{\mathrm{ED}}(\omega)|^2\omega^3}{3c^3\hbar\pi\varepsilon_0}\right)\left(\frac{n}{8\pi k_n^2}\right)\left(\frac{k_n}{k_1}\right)\left(\left|\frac{E_x}{E_0^{s,p}}\right|^2 + \left|\frac{E_y}{E_0^{s,p}}\right|^2 + \left|\frac{E_z}{E_0^{s,p}}\right|^2\right) \tag{4}$$

where c is the speed of light, $k_n$is the momentum, E_0 is the electric field amplitude of wave incident from medium whose refractive index is the n, $k_\perp$ is out-of-plane (OP) component of the momentum.

To generalize the emission rate for many number of emitting dipoles with their dipole moments oriented in $\hat{\imath}$ direction, the expression can be described as,

$$\Gamma_i^{s,p}(\omega, k_{II}) = C_0(\omega)\bar{n}_i|\mu_i(\omega)|^2\tilde{\rho}_i^{\mathrm{s,p}}(\omega, k_{II}), \text{ and} \tag{5}$$

$$C_0(\omega) = \frac{\omega^3}{c^3\hbar\pi\varepsilon_0}, \text{ and} \tag{6}$$

$$\tilde{\rho}_i^{\mathrm{s,p}}(\omega, k_{II}) = \left(\frac{n}{8\pi k_n^2}\right)\left(\frac{k_n}{k_\perp}\right)\left|\frac{E_i}{E_0^{s,p}}\right|^2 \tag{7}$$

Here, $\bar{n}_i|\mu_i(\omega)|^2$ is referred to as the dipole strength and $\tilde{\rho}_i^{\mathrm{s,p}}$ is called the local density of optical states (LDOS).

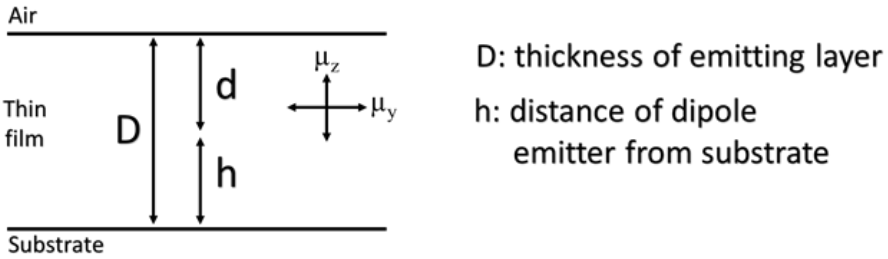

Figure 2. 15 Illustration of three-layer system of air, thin-film, and substrate.

As seen in Figure 2.15, an emitter is in the thin-film layer between air and substrate, and the emission is in the direction of y and z, defined as the in-plane (IP) and out-of-plane (OP), respectively.

In this system, the momentum in x direction is zero, $k_x = 0$, and the in-plane momentum, $k_{II} = k_y$, does not change in each layer. Therefore, the result of emission rate is based on k_y. As a result of the given in-plane momentum, the out-of-plane momentum is

$$k_{zi} = \sqrt{n_i^2 k_0^2 - k_y^2} \tag{8}$$

Fresnel equations, in terms of s and p-polarizations, in this system, are given by

$$t_{ij}^p = \frac{2n_i n_j k_{zi}}{n_j^2 k_{zi} + n_i^2 k_{zj}}, t_{ij}^s = \frac{2k_{zi}}{k_{zi} + k_{zj}} \tag{9}$$

$$r_{ij}^p = \frac{n_j^2 k_{zi} - n_i^2 k_{zj}}{n_j^2 k_{zi} + n_i^2 k_{zj}}, r_{ij}^p = \frac{k_{zi} - k_{zj}}{k_{zi} + k_{zj}} \tag{10}$$

As a result, the final s- and p-polarized LDOS are

$$p_{IP}^s(\omega, k_\parallel) = p_x^s(\omega, k_y) = \left(\frac{1}{8\pi k_0^2}\right)\left(\frac{k_0}{k_{z3}}\right)\left|\frac{t_{32}^s e^{ik_{z2}d}\left(1 + r_{21}^s e^{2ik_{z2}h}\right)}{1 - r_{21}^p r_{23}^p e^{2ik_{z2}D}}\right|^2 \tag{11}$$

$$p_{IP}^p(\omega, k_\parallel) = p_x^p(\omega, k_y) = \left(\frac{1}{8\pi k_0^2}\right)\left(\frac{k_0}{k_{z3}}\right)\left|\frac{t_{32}^p e^{ik_{z2}d}\frac{k_{z2}}{n_2 k_0}\left(1 + r_{21}^s e^{2ik_{z2}h}\right)}{1 - r_{21}^p r_{23}^p e^{2ik_{z2}D}}\right|^2 \tag{12}$$

$$p_{OP}^p(\omega, k_\parallel) = p_z^p(\omega, k_y) = \left(\frac{1}{8\pi k_0^2}\right)\left(\frac{k_0}{k_{z3}}\right)\left|\frac{t_{32}^p e^{ik_{z2}d}\frac{k_{z2}}{n_2 k_0}\left(1 - r_{21}^p e^{2ik_{z2}h}\right)}{1 - r_{21}^p r_{23}^p e^{2ik_{z2}D}}\right|^2 \tag{13}$$

So, the p-polarized and s-polarized luminescence can be written as

$$N^p(\omega, k_y) = C_{exp} C_0(\omega)[\tilde{\rho}_{IP}^p(\omega, k_y)\bar{n}_{IP}|\mu_{IP}(\omega)|^2 + \tilde{p}_{OP}^p(\omega, k_y)\bar{n}_{OP}|\mu_{OP}(\omega)|^2] \tag{14}$$

Using these equations, we can calculate luminescence data in the Fourier plane as seen in Figure 2.16.

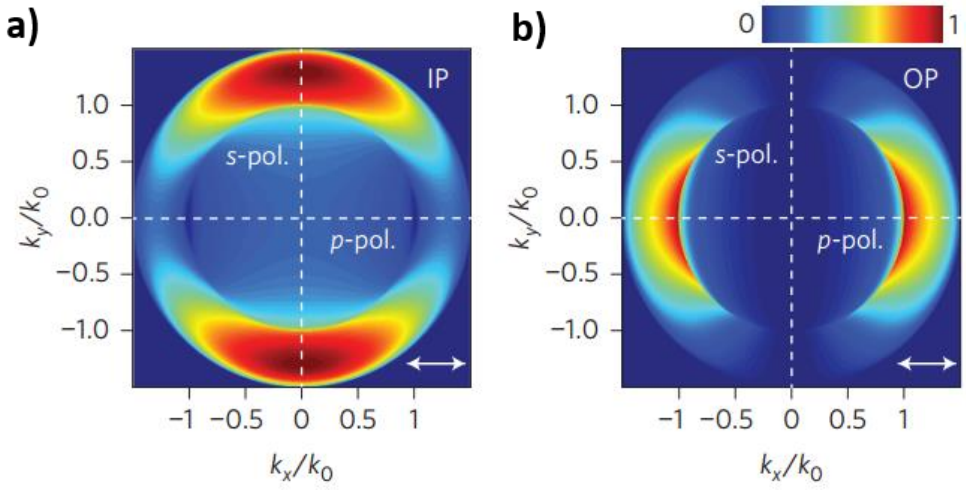

Figure 2. 16 Calculated back focal plane emission patterns of totally in-plane (a) and out-of-plane (b) transition dipole moments [41].

In the report of Scott *et al.*, the radiation pattern differences between CdSe nanoplatelets and colloidal quantum dots were reported using back focal plane imaging (see Figure 2.17) [42].

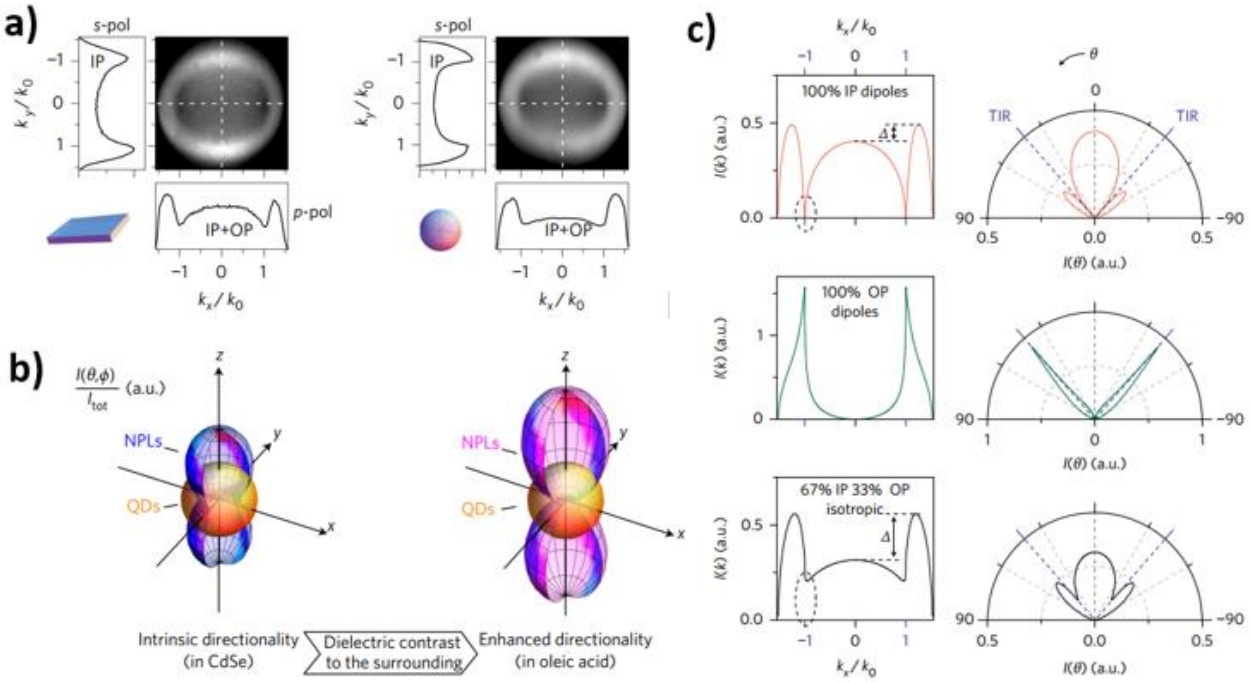

Figure 2. 17 Back focal plane emission of a monolayer oriented of nanoplatelets and colloidal quantum dots (a), radiation intensity pattern of nanoplatelets and quantum dots as shown in blue and orange colors, respectively (b), and calculated spectra of pure IP, OP, and isotropic distribution of IP and OP (c) [42].

This property of nanoplatelets makes them attractive for applications using self-assembly approach to control transition dipole orientation. Gao *et al.* showed ratio of in-plane and out-of-plane transition dipole moments of face-down and edge-up oriented self-assembled nanoplalet films [36], as mentioned in Figure 2.18.

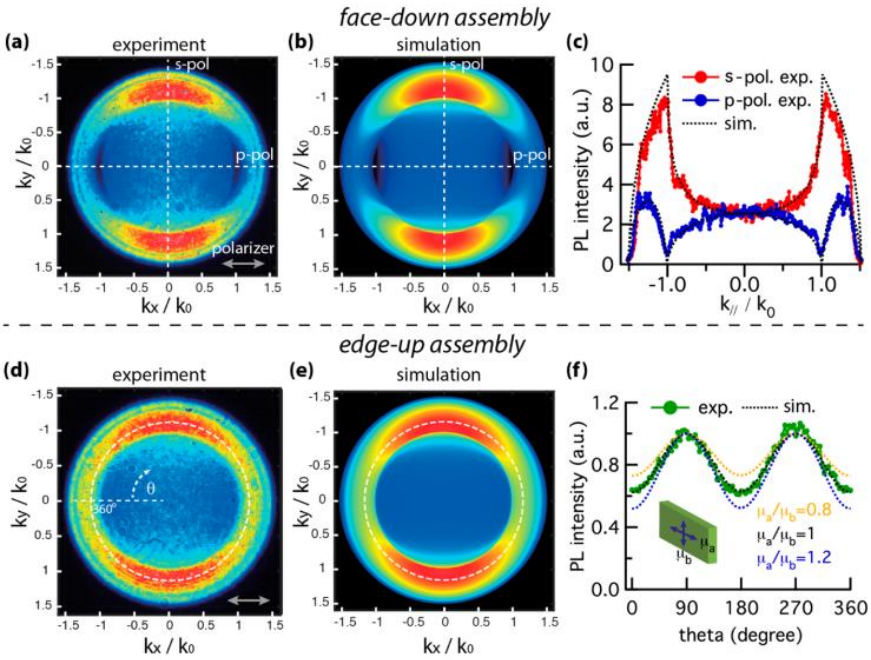

Figure 2. 18 Experimental (a) and calculated pure in-plane transition dipole moment (b) back focal plane images of face-down oriented CdSe nanoplatelets, and their comparisons on dashed line fitting spectra (c). Experimental back focal plane images of edge-up oriented CdSe nanoplatelets (d), calculated 50% in-plane and 50% out-of-plane transition dipole moments (e), and their comparisons on dashed line fitting spectra (f) [36].

In summary, colloidal quantum wells acquire advantages in versatile applications including solar concentrators [43], light-emitting diodes [44], and lasing [45] with emerging properties of step-like absorption spectrum profile, narrow emission bandwidth, large absorption cross-section and emission anisotropy, as compared to CQDs.

2.3. LIGHT-EMITTING DIODES (LEDs)

2.3.1. LEDs Operating Principles

Light-emitting diodes are electrically driven optoelectronic devices the emit light. LEDs include semiconductor materials as the emissive layer in which electrodes are using to inject electrons and holes driven by a current source. In operation, direct current (DC) can be applied, in forward bias in such a way that holes and electrons are injected through positive and negative electrodes, respectively. Injected electrodes and holes recombine radiatively in the semiconductors, releasing energy in the form of a photon. This phenomenon is called electroluminescence.

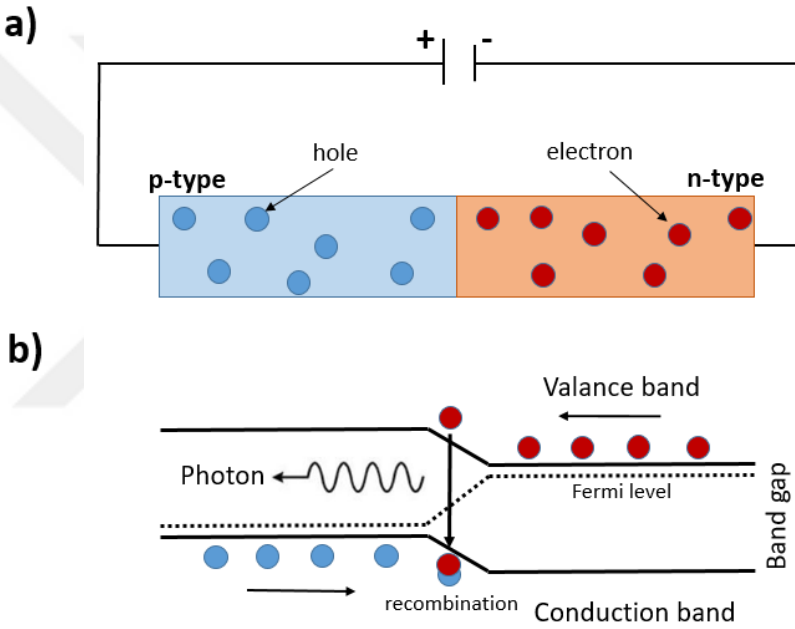

Figure 2. 19 Schematic diagram for the working principle of light-emitting diodes. The external circuit of light-emitting diodes (a), and the behavior of conduction, valance band, and electron/hole injection resulting in radiative recombination and photon emission in the forward bias (b).

In the emissive layer, a depletion region occurs with forward bias generating electron-hole pair (exciton) (see Figure 2.19). According to the effective energy band gap of the semiconductor, the released photon as a result of the electron-hole recombination has photon energy equal to the bandgap energy of this semiconductor used as the emissive layer. Semiconductor materials can have direct or indirect bandgap. As mentioned before, the semiconductor materials, having direct bandgap, the highest occupied energy level (HOMO) of valance band have the same momentum as the lowest unoccupied energy (LUMO) of conduction band on energy-momentum diagram. So, the bandgap theory states that the released energy in the form of photon is

$$\Delta E = h \cdot \nu = \frac{hc}{\lambda} \tag{15}$$

where h is the Planck's constant, ν is the frequency of light, c is the speed of light, and λ is the wavelength of light. Therefore, the effective bandgap energy of semiconductor materials determines the color of the emitted photon.

In the situation of indirect bandgap semiconductors, photons do not obtain emitted, since HOMO and LUMO levels do not match in the momentum.

2.3.2. LED Architecture

The simplest structure of LEDs includes an emissive layer (EML) sandwiched between anode and cathode as seen in Figure 2.20a, but this structure is not effective in injecting electrons and holes into the emissive layer because of the energy barriers in the interfaces (see Figure 2.20b). To form an exciton in EML, engineering the structure of LEDs is needed. This engineering includes building gradual and stepwise energy level profile to ease up injection of electrons and holes into EML, and in the same time, to inhibit undesirable charge movement and block nonradiative radiation. In this regard, LEDs structures (see Figure 2.21) comprise electron and hole injection and transport layers (ETL, EIL, HTL, HIL) [46].

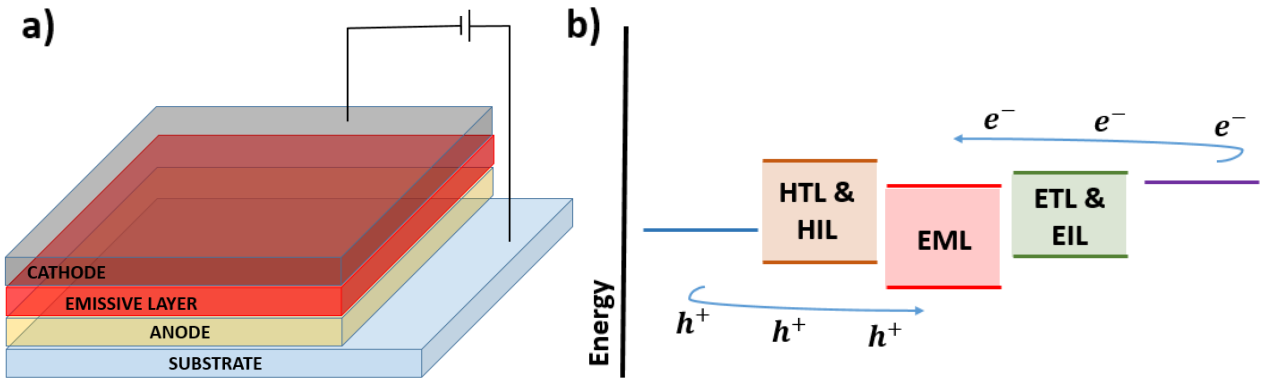

Figure 2. 20 Schematic illustrations of the simplest LED structure (a) and the corresponding energy band diagram (b).

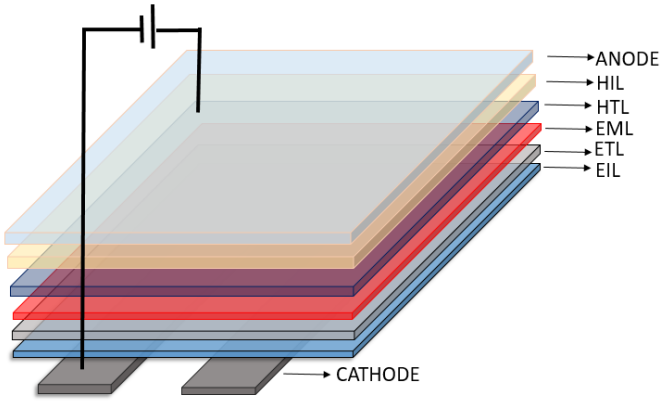

Figure 2. 21 Illustration of an advanced structure of LEDs.

Transparent indium tin oxide (ITO) can be often used as anode and cathode in optoelectronic applications, since the optical and electronic properties of ITO is favorable to achieve high transparency to propagate light, high charge mobility and conductivity, and matching range of work functions [46]. On the other hand, metallic electrodes, such as gold, aluminum, and silver, are also commonly used for LED applications [47].

Hole injection layers serve as a kind of p-type semiconductors with high hole mobility and Fermi level close of metal or ITO electrodes for the injection of holes through transport layer. Commonly used materials for HIL are poly(3,4-ethylene dioxythiophene): polystyrene sulfonate (PEDOT: PSS) [48] and molybdenum oxide (MoO3) [49] as organic and inorganic semiconductor materials, respectively. Hole transport layers are intermediate layers that transport holes from HIL to EML for the purposes of providing reduced energy barrier for positive charges, and blocking electron transfer through the anode. Poly(9-vinylcarbazole) (PVK), Poly(4-butyl-N,N-diphenylaniline) (p-TPD), and 4,4′-Bis(N-carbazolyl)-1,1′-biphenyl (CBP) are generally used as HTL.

Electron injection and transport layers, similar to HIL and HTL, are used for the electron injection to EML with high electron mobility values. Materials for EIL and ETL include lithium fluoride (LiF), zinc oxide (ZnO) and titanium oxide (TiO_2) [50].

In LED structures, direct bandgap semiconductor materials are used for the radiative recombination of electrons and holes. EML is the main part of LEDs. Colloidal quantum dots (CQDs), perovskites, and colloidal quantum wells (CQWs) are effective semiconductors materials used as EML. A critical property of EML materials is high photoluminescence quantum yield (PLQY), which directly affects the efficiency of LEDs, as given by

$$\Phi = \frac{number\ of\ emitted\ photons}{number\ of\ absorbed\ photons} \tag{16}$$

where Φ is PLQY of material. For effective EML, PLQY should be high in the film form. Morphological and chemical uniformity, and low defects may be critical on the efficiency of LEDs.

Based on the LED architecture and fabrication methods, there are two main types of LEDs, which are the conventional (normal) structure and the inverted structure (see Figure 2.22), constructed using solution-based and evaporation-based processing, respectively [46]. According to the device architecture of LEDs, hole and electron transport/injection layers can be swapped.

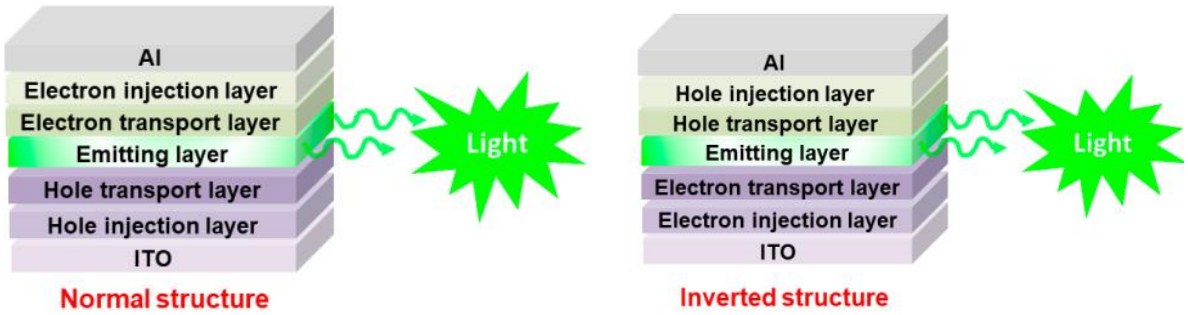

Figure 2. 22 Schematics of the normal and inverted structures of LEDs [46].

In solution-based methods, materials are used in liquid form, and some of the used deposition techniques are spin-coated [51] and drop-casting [52]. Spin-coating method is commonly used for deposition and the parameters such as thickness and uniformity depended on the prescribed speed and concentration of solutions. This is the most preferred method because of its low cost. On the other hand, evaporation-based deposition of layers is relatively costly because of the requirements of high vacuum environment. However, uniformity of films, reduced defected areas, and precise control of the thickness of layers are its advantages.

2.3.3. Characterization of LEDs

The most important figure-of-merit measured to describe LED performance is the external quantum efficiency (EQE). The EQE is defined as the ratio of photons collected from an LED to the number of electrons driven in the LED by the external circuit. EQE can be calculated theoretically based on the internal quantum efficiency (IQE) as follows

$$IQE = r \cdot q \cdot \gamma \tag{17}$$

$$EQE = \eta_{out} \cdot IQE \tag{18}$$

Here, r is the fraction of excitons that go through radiative recombination, q is PLQY of the emissive material in the thin-film, γ is charge injection efficiency, and η_{out} is the outcoupling efficiency.

There are three approaches to measure EQE of LEDs. One method using a large photodetector in front of an LED to collect photons emitted into the upper hemisphere is the easiest way to measure of EQE (see Figure 2.23a). However, this method may lead to some misreading of out-coupled light. A second approach is to use a photodetector mounted on a goniometer at a distance from the emitting area (see Figure 2.23b). For both of these ways, the Lambertian assumption of radiation pattern is required. This assumption may lead to overestimation of EQE values. In the third method, an integrating sphere and a spectrometer are used to collect all photons (see Figure 2.23c). This is the most accurate way to eliminate errors coming from angular dependency of photon emission and detection.

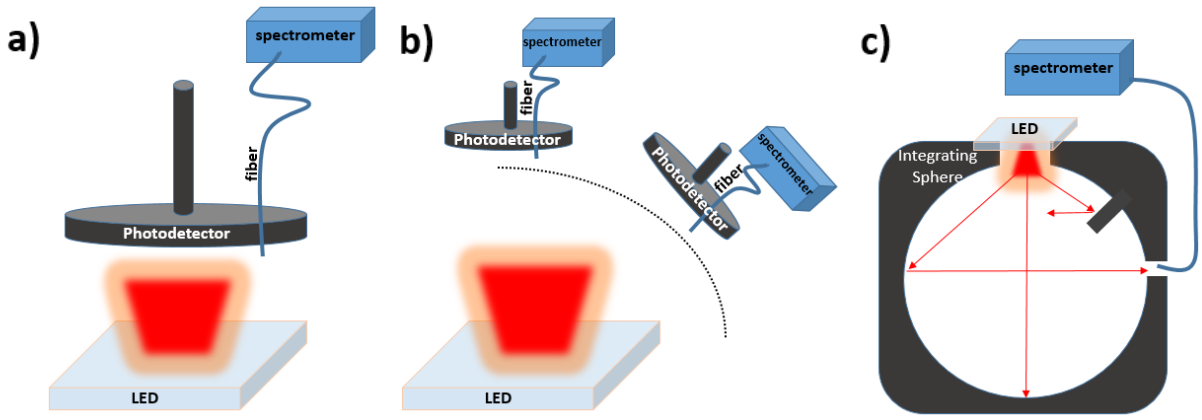

Figure 2. 23 EQE measurement method in which a large photodetector is placed on an LED (a), and a photodetector is mounted on a goniometer to measure the angular distribution of the emission from an LED (b), and a LED is placed in an integrating sphere (c) with a spectrometer to measure the spectral power information.

Luminance is a quantity based on the light intensity of an LED in unit area, measured by using spectroradiometer in a direction. The international unit of luminance is candela per square meter (cd/m^2). The International Commission on Illumination (CIE) describes color spectrum of light given in the wavelength range which human eye detect. In Figure 2.24, conventional CIE diagram is shown representing tones of red, green, and blue color in the visible range [53].

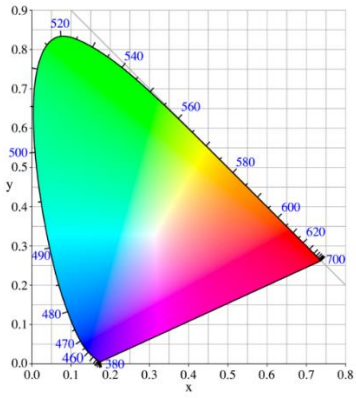

Figure 2. 24 Conventional CIE diagram [54].

The current density vs. voltage behavior is a critical metric to evaluate the performance of LEDs, describing charge flow in device per applied voltage. In the diagram of current density-voltage (J-V), increasing voltage increases current density after the turn-on voltage (see Figure 2.25).

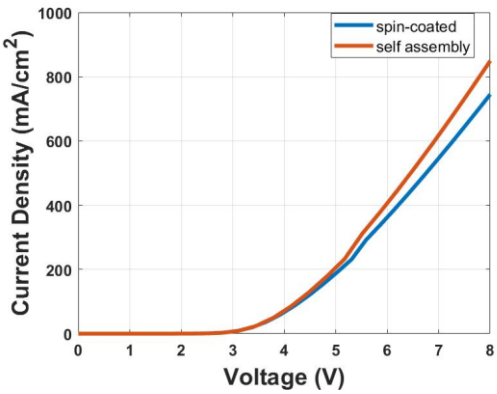

Figure 2. 25 J-V characteristics.

The lifetime of LEDs is the period of time that takes for the initial luminance value of an LED, generally 100 cd/m^2, to decrease to the half of that starting point. Lifetime is denoted as T_{50}. Instead of using the starting with 100 cd/m^2, T_{50} can be estimated for any origin by using the relation as

$$L_0^n T_{50} = L_1^n T_{50} \qquad (19)$$

where L_0 is the initial luminance value, L_1 is 100 cd/m^2, and n is the acceleration factor [55]. However, it is typically difficult to obtain an accurate value. The lifetime of LEDs can be affected by some factors such as the stability of materials and charge transporting in device.

CHAPTER 3

3 EXPERIMENTAL METHODS

In this chapter, the experimental methods including the synthesis of CQWs, ZnO, and ZnMgO, self-assembly process, fabrication of CQW-LEDs, and characterization techniques of the CQWs and LEDs are presented.

3.1. Synthesis of Materials

3.1.1. Cadmium Myristate

The colloidal quantum well used in this project are in the form of core/shell CdSe/CdZnS. The core of CdSe starts with the synthesis of cadmium myristate (Cd(myr)). In this work, the Cd(myr) is synthesized with slight modifications of the recipe, previously reported by Altintas *et al.* [56]. In this synthesis, 2.46 g of cadmium nitrate dissolved in 80 mL of methanol and 6.26 g of sodium myristate dissolved in 500 mL of methanol are mixed and kept stirring for 5 h. The resulting solution is precipitated by centrifugation, and washed twice with methanol. The final white color product is kept under vacuum at room temperature during night. The synthesized Cd(myr) should be stored in refrigerator at about 4 ^{0}C.

3.1.2. 4.5 ML CdSe Core CQWs

After preparation of Cd(myr), 4.5 ML CdSe core is synthesized according to the previous reports [57]. In the synthesis, first 24 mg of Se powder and 340 mg of cadmium myristate are dissolved in 30 mL of octadecene (ODE) into 100 mL three-neck flask at 92 ^{0}C under vacuum. After 1 hour, the temperature is set to 240 ^{0}C under argon gas. During this process, 120 mg of cadmium acetate dehydrate is added at 192 ^{0}C, and when the temperature reaches 210 ^{0}C, the resulted solution is stirred for 7 min. After then, 1.5 mL oleic acid (OA) is added into solution, and the solution is directly quenched in cold-water bath. The synthesized NCs is washed 2 times, firstly with hexane, and secondly with ethanol for purification of 4.5 ML CdSe core CQWs. Finally, CQWs is dispersed in hexane.

3.1.3. CdSe/CdZnS Core/Hot-Injection Shell (HIS) CQWs

We synthesized CdSe/CdZnS core/shell nanoplatelets based on the previous report of Demir's Research Group [57]. Four optical density synthezised 4.5 ML CdSe core, 55 mg zinc acetate, and 22.5 mg cadmium acetate are dissolved in 7.5 mL ODE and 1 mL OA into 50 mL three-neck flask at room temperature under vacuum for 1 hour. Then, the temperature is set to 80 ^{0}C, and the solution is stirred for 1 h. After that, under argon gas, temperature is set to 300 ^{0}C, and prepared precursor, including 5 mL ODE and 140 μL octanethiol, is started to be injected at 165 ^{0}C at a rate of 10 mL/h. The rate should be decreased to 4 mL/h after the temperature reaches 240 ^{0}C. After injection is completed, the reaction is terminated by quenching in cold-water bath. The synthesized NCs is washed 2 times, firstly with hexane, and secondly with ethanol for purification of CdSe/CdZnS core/HIS CQWs. Finally, CQWs is dispersed in hexane.

3.1.4. ZnO and ZnMgO Nanoparticles

ZnO and ZnMgO nanoparticles are commonly used electron injection layer for LEDs. In our LED structure, we used them as ETL and EIL. ZnO nanoparticles are synthesized according to the literature [58]. Dimethyl sulfoxide (DMSO) of 30 mL and $Zn(CH_3COO)_2$ of 3 mmol, and ethanol of 10 mL and tetramethylammonium hydroxide (TMAH) of 5 mmol are stirred until dissolution is completed. Then, the ethanol solution is injected into DMSO solution at the rate of 40 mL/h. After injection is completed, the resulted solution is stirred for 24 hours under ambient conditions. After 24 hours, ZnO

nanoparticles is precipitated with ethyl acetate of 65 mL, and dissolved in ethanol. While the ethanol solution of ZnO nanoparticles is stirred, 160 μL 2-ethanolamine is directly injected into solution to stabilize the NCs. Finally, the final solution is washed with ethyl acetate and redispersed in ethanol in a volume for available density. The solution of ZnO is filtered before used.

Mg doped ZnO ($Zn_{0.95}Mg_{0.05}O$) nanoparticles are synthesized based on report of Alexandrov *et al.* [59] with some modifications. DMSO of 30 mL and $Zn(CH_3COO)_2$ of 2.95 mmol and 0.05 mmol magnesium acetate tetrahydrate, and 10 mL ethanol and 5.5 mmol tetramethylammonium hydroxide (TMAH) are stirred until dissolution is completed. Then, the ethanol solution is injected into DMSO solution at the rate of 40 mL/h. After injection is completed, the resulted solution is stirred for 24 hours under ambient conditions. After 24 hours, Mg doped ZnO nanoparticles are precipitated with 65 mL ethyl acetate, and dissolved in ethanol. While the ethanol solution of Mg doped ZnO nanoparticles are stirred, 160 μL 2-ethanolamine is directly injected into solution to stabilize the nanoparticles. Finally, the final solution is washed with ethyl acetate and redispersed in ethanol in a volume for available density. The solution of Mg doped ZnO nanoparticles are filtered before used.

3.2. Self-Assembly of CQWs for their Face-Down and Edge-Up Orientation

For liquid-interface self-assembly, the synthesized CdSe/CdZnS core/HIS CQWs are dispersed in either hexane and octane for certain concentrations. The stocked dispersion of CQWs in hexane is removed from hexane with centrifuge of solution added into ethanol, and precipitated CQWs is redispersed in the solvent. All self-assembly processes are carried out at room temperature. For the self-assembly processes, a Teflon cap whose radius is 5 cm and depth is 3 cm. The Teflon cap has a hole on the well for the removal of the subphase, slowly by using a syringe. Inside the Teflon cap, a tilted glass holder is placed as a platform for the substrate to sit as seen in Figure 3.1.

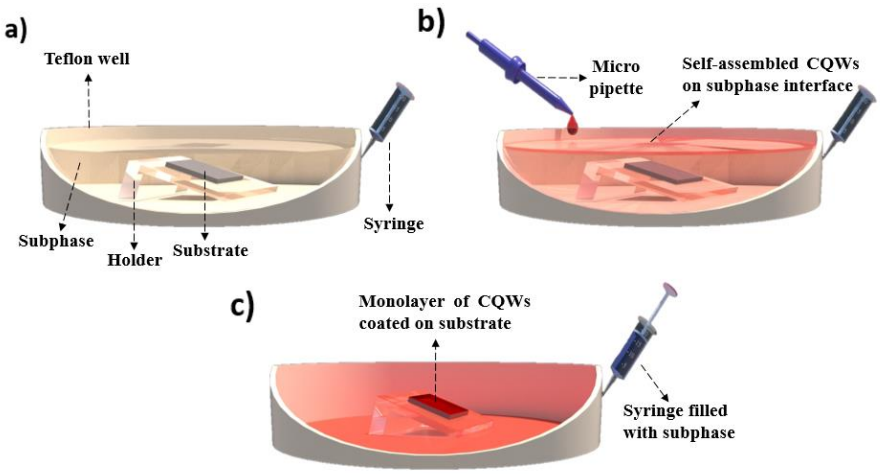

Figure 3. 1 Self-assembly process on liquid interface. Subphase is filled into Teflon well (a), on top of the subphase, CQWs solution is dropped (b), and subphase is removed by a syringe (c).

The Teflon cap is filled with the available amount of subphase, and various volumes of CQWs are dropped on top of the subphase. Then, after adding CQWs, the cap is covered with a petri dish to slow down evaporation rate of the solvents, and a certain period of time is waited to form oriented film. For allowing for deposition of the oriented film on a substrate, the subphase is slowly removed utilizing a syringe that is inserted into the Teflon well's side. To get rid of the residual subphase, the substrate is further vacuumed in a chamber for sufficient period of time.

In controlling the orientation of self-assembled CQW films, the affecting factors are the polarity differences between solvents of CQWs and the subphase, evaporation rate of the solvents, and concentration and dropping amount of the CQWs solutions. During a self-assembly process, each of these factors is controlled while a chosen factor is varied and the others are held constant.

The most important factor on the orientation of self-assembled CQW film is the type of the solvent of CQWs. For face-down oriented self-assembled film, hexane is used as the solvent while octane is used for the edge-up one (see Figure 3.2). The type of solvent has direct influence on the evaporation rate which is of hexane (0.103 $\mu L/s \cdot cm^2$) and of octane (0.018 $\mu L/s \cdot cm^2$) [38].

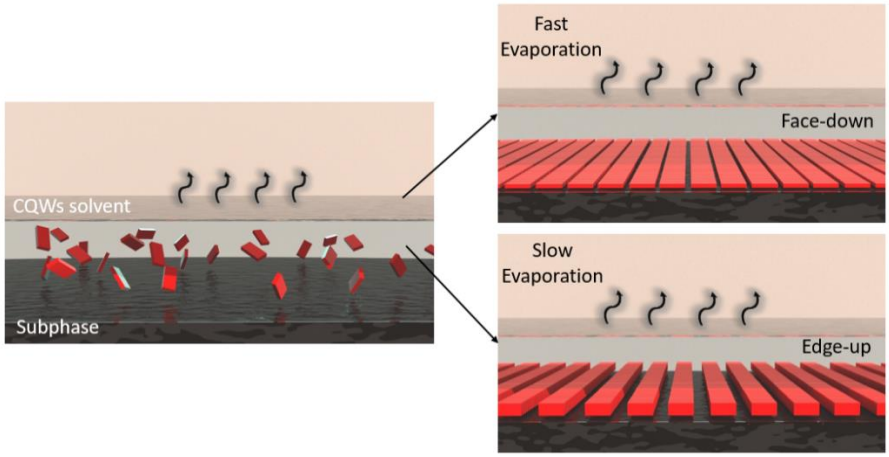

Figure 3. 2 Schematic diagram of effect of the evaporation rate of solvent on the orientation of self-assembled CQW film.

The evaporation rate is not only effective on the orientation, at the same time the type of subphase used is critical during the self-assembly processes in which acetonitrile, diethylene glycol, and ethylene glycol have been used as the subphase in our studies thus far (see Figure 3.3). Since stronger intermolecular forces and polarity differences between the subphase and the solvent is required, based on used these solvents, a desired available subphase is chosen.

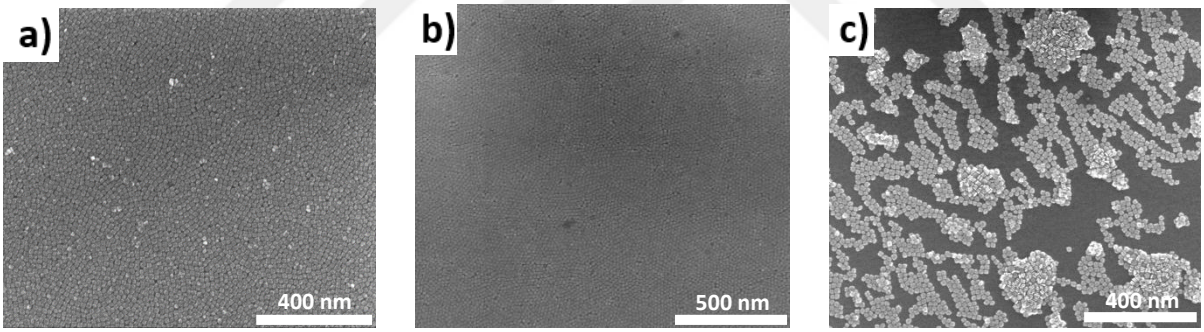

Figure 3. 3 SEM images of our self-assembled films of CdSe/CdZnS core /HIS CQWs on Si substrates. Here, the solvent of CQWs used is hexane, and the subphases are acetonitrile (a), diethylene glycol (b), and ethylene glycol (c). Note that for each sets, the concentration of CQWs solution is 20 mg/mL and the amount of droppings is 20 µL in each case.

The other factors for the self-assembly processes are the concentration and dropping amount of CQWs solutions. These factors affect the orientation and surface coverage of the resulting self-assembled films. In Figure 3.4, examples of the face-down oriented self-assembly process sets are shown in which the concentrations of CQWs solution in hexane used are 10, 20, and 30 mg/mL, and the dropping amount of 20 µL is employed.

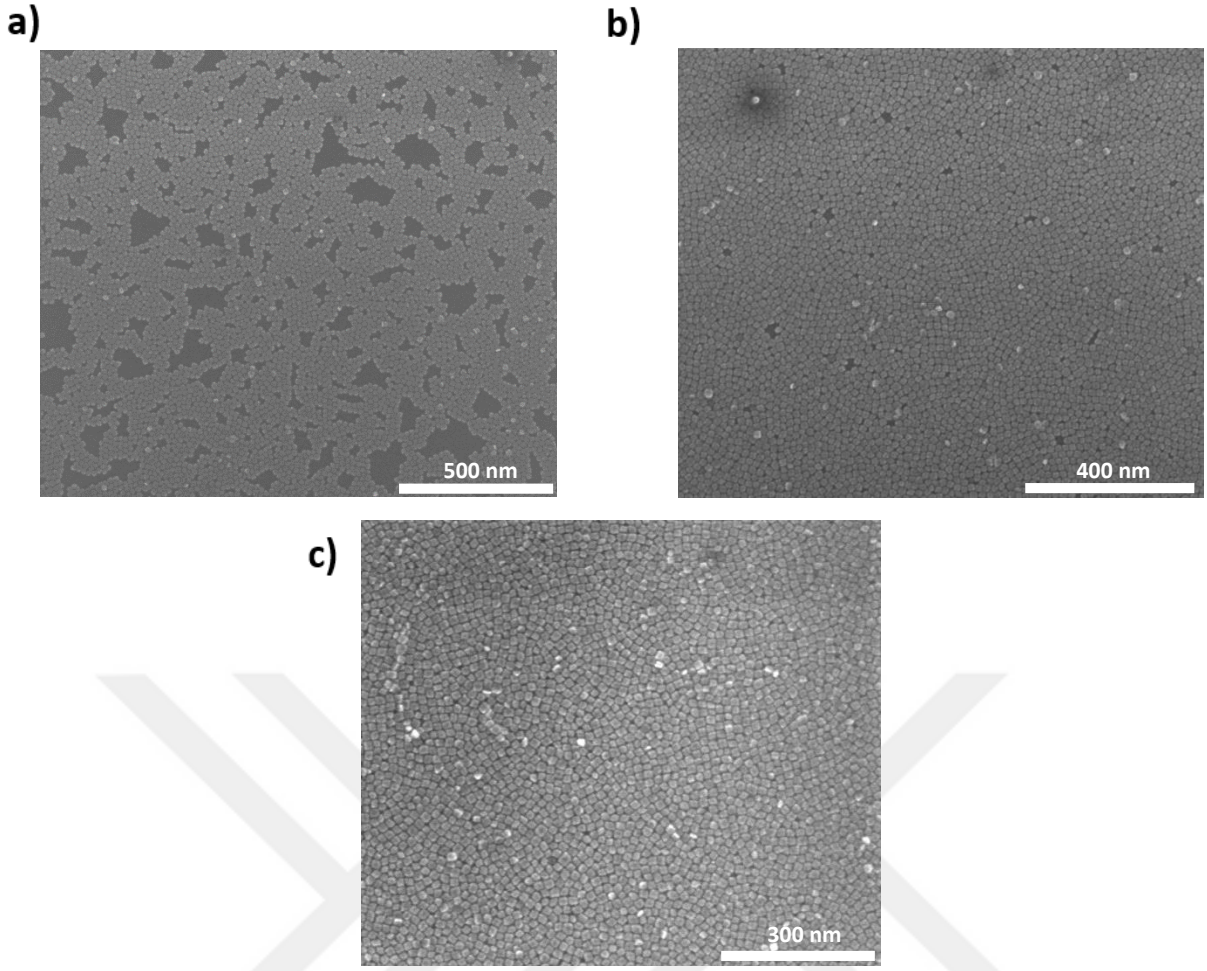

Figure 3. 4 SEM images of our self-assembled films of CdSe/CdZnS core /HIS CQWs on Si substrates. Here, the solvent of CQWs used is hexane, and the subphases are acetonitrile, while the concentration of CQWs solution is varied: 10 mg/mL (a), 20 mg/mL (b), and 30 mg/mL (c). Note that for each set, the amount of dropping is 20 µL.

The adjustment of solvents, subphase, and concentration of CQWs solution has shown that all edge-up orientation self-assembled film requires using the subphase of ethylene glycol, the solvent of octane, and the concentration of CQWs solution at 20 mg/mL as presented in Figure 3.5a. On the other hand, all face-down oriented self-assembled film requires the use of acetonitrile as the subphase, hexane as the solvent, and the CQWs solution of 17 mg/mL in concentration as shown in Figure 3.5b. Moreover, for the edge-up oriented film, after dropping CQWs solution on the subphase, a petri dish is covered on the Teflon well, and after waiting for 40 min, the petri dish is held for 20 min to complete the evaporation of octane before removing all subphase. Additionally, for the face-down oriented film, both of acetonitrile and diethylene glycol can be used, but after completing self-assembly process, evaporation of diethylene glycol takes much longer than acetonitrile.

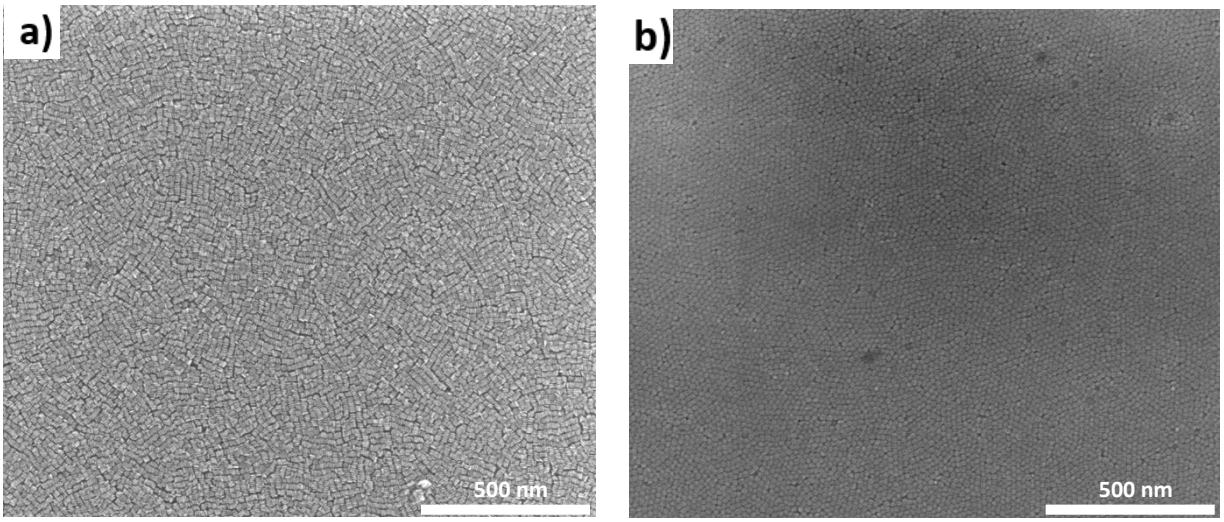

Figure 3. 5 Optimized all edge-up (a) and face-down (b) orientated self-assembled CQW films on Si substrate.

3.3. LED Device Fabrication

The first step of LED fabrication is the cleaning of substrates. We have used patterned indium tin oxide (ITO) coated glass as the substrate purchased from Ossilla (see Figure 3.6). The thickness of ITO is 100 nm while the thickness of glass is 1.1 cm in total. The cleaning process of these substrates starts with the substrates being sonicated in a solution of Hellmanex dissolved in distilled water with a ratio of 1:10 for 10 min. After that, substrates are cleaned under running distilled water. The same procedure is repeated in acetone and then isopropanol baths. This cleaning process provides cleaning of all physical contaminations on a substrate.

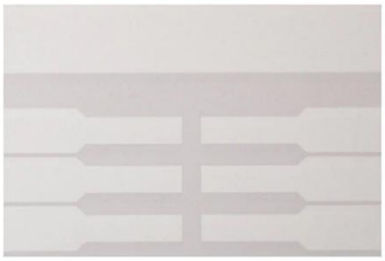

Figure 3. 6 ITO coated glass substrate used in this thesis work.

After cleaning process, substrates are treated by ozone-plasma (Asher Ozon-plasma instrument) which is capable of breaking down organic surface contaminants to obtain near-atomically clean surfaces. The ozone-plasma treatment is produced at 30 W and applied for 10 min.

Layer deposition processes have some differences for the normal and inverted structures of LEDs. During our work, both of these structures were studied. Firstly, for normal structure LEDs, the hole injection layer (HIL) is deposited on an ITO coated substrate by spin-coater. This HIL is made of a solution of PEDOT:PSS dissolved in isopropanol with one-to-one ratio. Before spin-coating, PEDOT:PSS solution is filtered with 0.45 μm hydrophilic filters. The parameter of spin-coating process under environmental conditions is 3,000 rpm for 45 s. After deposition, the substrate is annealed at 120 ^{0}C for 30 min, and then transferred to nitrogen-filled glove box ($O_2 < 0.1\ ppm\ and\ H_2O < 0.5\ ppm$). Before the deposition of hole transporting layer, poly-TPD and PVK solutions are prepared. Poly-TPD is dissolved in chlorobenzene and stirred for 24 h, and the concentration of solution is 8 mg/mL. PVK is dissolved in dioxane, and the concentration of solution is 2 mg/mL. When the solutions are ready, poly-TPD solution is spin-coated at 2,000 rpm for 60 s, and annealed at 110 ^{0}C for 30 min. Then, PVK solution is spin-coated at 2,000 rpm for 60 s, and annealed at 150 ^{0}C for 20 min. All spin-coated processes are performed in dynamic mode.

After hole layer deposition, the emissive layer is deposited with spin-coating or self-assembly method. For spin-coating, CQWs solution in hexane is prepared at a concentration of 10 mg/mL, and the solution is spin-coated with 3,000 rpm for 45 s, and then baked on a hot plate at 80 ^{0}C for 10 min. For all face-down self-assembly, as mentioned in the previous part, as the subphase, acetonitrile is used, and the solvent of CQWs is hexane. After completing all face-down oriented self-assembly process, the substrates are vacuumed for evaporation of acetonitrile in its entirely. Following EML, the electron injection and transporting layer (EIL, ETL) of ZnMgO solution in ethanol with 25 mg/mL concentration was spin-coated at 3,000 rpm for 60 s, and baked at 90 ^{0}C for 30 min.

For deposition of Al layer as the cathode, the substrate is transferred to thermal evaporation system of which pressure level is around 10^{-7} Torr. For deposition of Al layer, a hard mask with an active area of 4.5 mm^2 is used. The deposition rate of Al is around 5 ^{0}A/s, and the thickness is 100 nm.

After completed deposition of all layers, to product LEDs from moisture and oxygen, devices are encapsulated by glass coverslip sticked by UV-curable resin.

For inverted-structure LEDs, the ETL of ZnO is spin-coated on an ITO coated substrate with parameters of 3,000 rpm for 60 s, and baked at 110 ^{0}C for 30 min. After that, EML is deposited with spin-coating, face-down and edge-up orientation self- assembly methods. Spin-coating and face-down self-assembly processes are the same with those of normal structure LEDs. For all edge-up oriented

self-assembled EML, as mentioned in the self-assembly part, ethylene glycol is used as the subphase, and the solvent of CQWs is octane. Unlike face-down self-assembly process, after completing edge-up self-assembly process, substrates are kept in the vacuum chamber for around 12 h for complete evaporation of the subphase.

After deposition of EML, the substrate is transferred to thermal evaporation system with a hard mask. For inverted-structure LEDs, all HIL and HTL of CBP and MoO_3 are deposited with thermal evaporation system at a pressure level of around 10^{-7} Torr. The evaporation rates are 0.5 A^0/s for both hole layers. The thicknesses of CBP and MoO_3 are 60 and 8 nm, respectively. For anode layer, Al is used, and the processes of deposition of cathode and encapsulation are the same as the processes of normal structure LEDs.

3.4. LEDs Characterization

In this section, the methods for analyzing synthesized CQWs, deposited layers and LEDs are discussed. For excitonic light-matter interaction properties of CQWs, optical spectroscopies are used. A UV-Vis-NIR spectrophotometer is used to measure the absorption spectrum of CQWs. For light emission properties of CQWs, a spectrometer and an integrating sphere are used to obtain photoluminescence (PL) spectrum and photoluminescence quantum yield. For PL and absorption measurements, Cary 5000 UV-Vis-NIR Spectrophotometer is employed. For the measurement of PLQY, the ratio of emission versus absorption intensity, and the emission collected from the sample in integrated sphere is recorded by spectrometer. Fourier-transform infrared spectroscopy (FTIR) measures the bonds profile of CQWs in infrared region. For description of ligands of CQWs, FTIR measurement technique is used.

The imaging techniques for CQWs and other layers are available with transmission electron microscopy (TEM), scanning electron microscopy (SEM), atomic force microscopy (AFM), and back focal plane (BFP) imaging.

The BFP measurements describe the transition dipole moment profile of CQWs in film, as discussed in scientific background part. The actual photograph of BFP setup is shown in Figure 3.7. In this setup, a 405 nm laser beam is used to excite CQWs films, and the setup consists of an inverted microscope with an infinity-corrected 1.3 numerical aperture (NA), oil-immersed Nikon objective. The Fourier plane image consists of reverse side of the oil-immersed objective, recorded by a CCD camera.

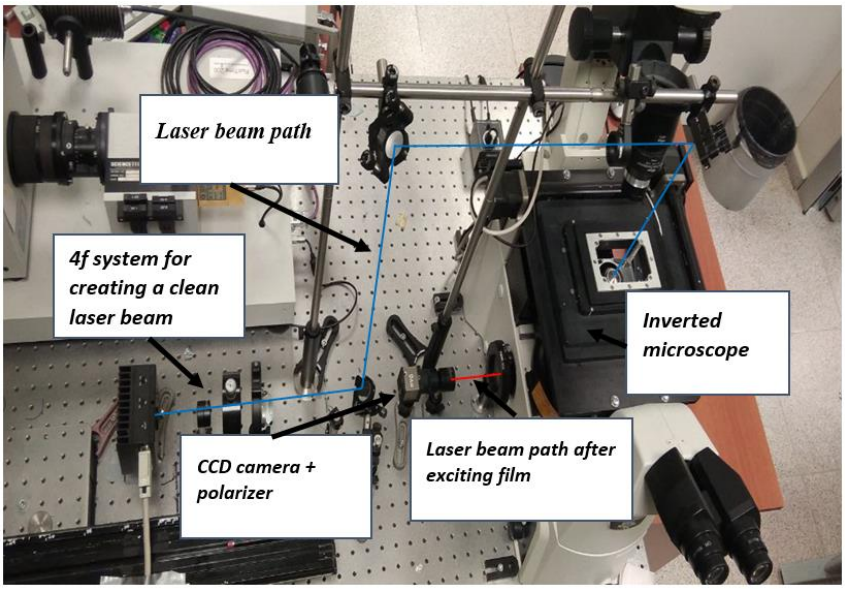

Figure 3. 7 Photograph of our BFP setup.

The schematic diagram of our BFP setup and the optical path of our beam is shown in Figure 3.8. After exciting the sample, photons are collecting by our oil-immersed objective and the collected infinite beam after the oil-immersed objective is focused to a Bertrand lens, which is a convergent lens to focus on the CCD camera's detection plane.

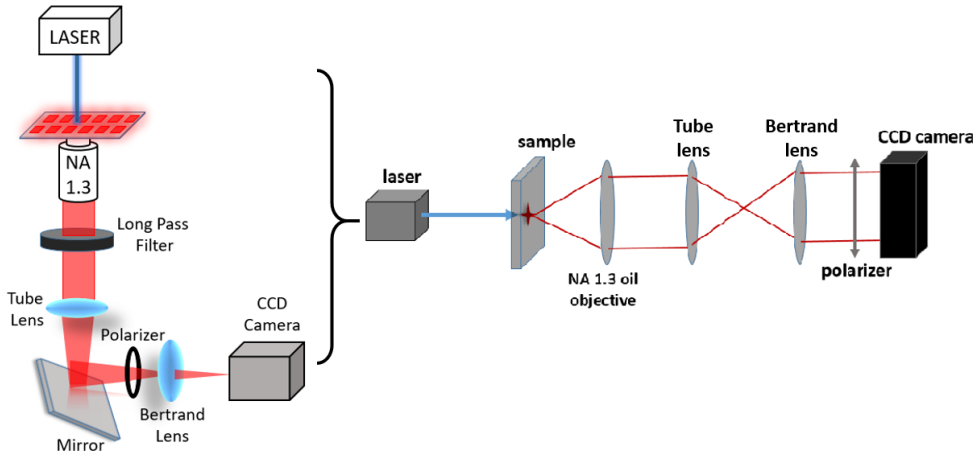

Figure 3. 8 Schematic diagram of our BFP setup and the trace of optical beams.

Light-extraction efficiency (LEE) and theoretical angular emission intensity calculations of the LED structure are carried out using the finite-discrete time-domain (FDTD) method. Simulations are conducted by utilizing commercially available Lumerical FDTD Solutions (ANSYS Inc). To simulate the structure properly, thicknesses and refractive indices of each layer were determined by

ellipsometric measurements. The active region of the LED, which consists of NPLs, is modeled as electric dipoles. For simulation dipoles are placed in the center of the active layer. Metal boundary condition is used on the verge of the cathode layer. All the other boundary conditions are selected as perfectly matched layer (PML), which serve as perfect light absorbers, so that fields radiated in the structure do not reach the absorbing boundaries. FDTD calculation was carried out in a limited volume of 10×10×2.29 μm. To obtain the angular distribution of light in the substrate, the far-field projection is calculated using the following formula

$$E_{far}(\theta,\varphi) = -\sqrt{-\frac{i}{8\pi k}}\frac{e^{-ikr}}{\sqrt{r}}\int(\omega\mu_0 H(r') + kE(r')sin\theta)e^{ikr'cos\varphi}dl' \quad (20)$$

where k is the wavenumber, r' is the distance between the source and near-field monitor, r is the distance between the source and far-field region, ω is the angular frequency and μ_0 is the permeability of free space. From incident electric field and transmission coefficients, founded by Fresnel equations, the angular distribution of emitted light in the air is found. The extracted power is determined by the following equation

$$P_{ext} = \frac{1}{2}\sqrt{\frac{\epsilon_0}{\mu_0}}\iint|E_{air}(\theta,\varphi)|^2 sin(\theta)d\theta d\varphi \quad (21)$$

where $E_{\text{air}}(\theta,\phi)$ is the electric field in the air with a specific direction angle.

Total extracted optical power from both the orientation controlled and the random-oriented structures are calculated by repeating the above analysis for three fundamental dipole directions in ‘x’, ’y’, and ‘z’. It can be seen that the ‘x’ and ‘y’ orientations are parallel to the CQW plane while the ‘z’ orientation is perpendicular. To calculate light-extraction efficiency, the results of each of these three analyses are multiplied with the ratio of dipoles in a specific orientation to all dipoles, their squares are added to each other, and divided by average dipole power [60].

To evaluate device performance, characterization techniques of external quantum efficiency (EQE), current density-voltage (J-V), electroluminescence (EL), luminescence (L) are used. Measurements of EQE, J-V, and EL are provided using a homemade computer-based system consisting of integrated sphere connected with Ocean Optics (QE-Pro) spectrometer with a fiber, and Agilent Technologies (U3606A) power source. The software directly gives EQE and current density values based on varying voltage and EL intensity over the optical wavelength.

To measure luminescence, Konica Minolta CS-200 spectroradiometer is used and luminescence values are recorded in unit of cd/m^2. The CIE coordinates of emitted light from active region of LEDs are also measured.

CHAPTER 4

4 RESULTS AND DISCUSSION

This chapter covers the measurements and analyses as well as the simulations, whenever applicable, of optical and electrical characteristics of CQWs and their LED devices. A part of this thesis is taken from our own paper by H. Dehghanpour Baruj*, Iklim Bozkaya*, Betul Canimkurbey*, A. Tarik Isik, Farzan Shabani, Savas Delikanli, Sushant Shendre, Onur Erdem, Furkan Isik, and H. Volkan Demir, "Highly-Directional, Highly-Efficient Solution-Processed Light-Emitting Diodes of All-Face-Down Oriented Colloidal Quantum Well Self-Assembly" (* equal contributor) [61].

4.1. All-Face-Down Oriented Colloidal Quantum Well Based Light-Emitting Diodes

In this thesis work, we used CdSe/$Cd_{0.25}Zn_{0.75}S$ core/hot-injected shell (HIS) grown CQWs high photoluminescence quantum yield (PLQY), which was previously demonstrated by our group [5]. The used CdSe cores have square-shaped geometry, and a gradient shell is grown on the seeds with surface ligands of oleic acid (OA) and oleylamine (OLA). As mentioned in the scientific background, the growth shell confines the wave function into the core region, which inhibits nonradiative recombination on surface traps. Moreover, the ligands of OA and OLA ensure good solubility and stability of CQWs in their solvents. Their heterostructure is the primary factor contributing to a high PLQY of 95% in solution and 87% in film form in a saturated deep-red color. Figure 4.1 shows TEM image of this core/HIS CQWs.

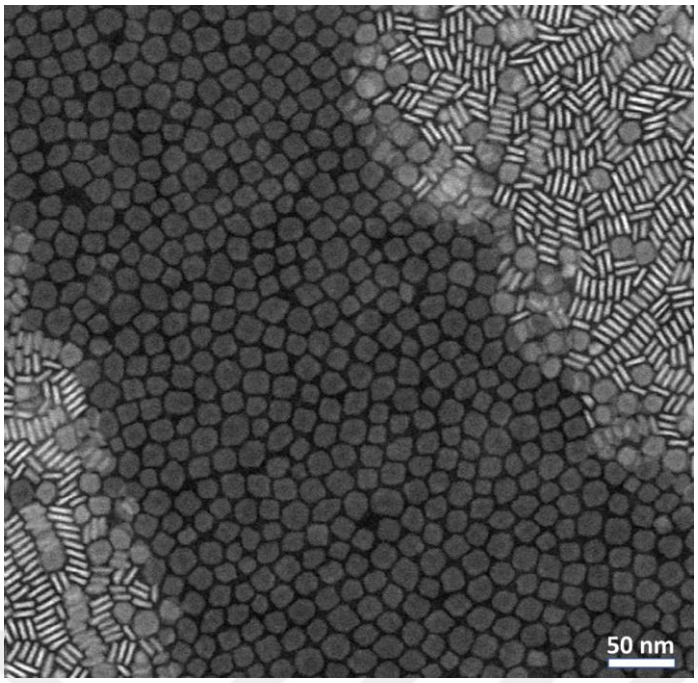

Figure 4. 1 TEM image of our hot-injection shell grown CQWs. The face-down and edge-up orientations of these CQWs co-exist in this image.

As shown in Figure 4.1, CdSe/CdZnS core/HIS CQWs have large lateral area and ultrathin vertical thickness of few nanometers, allow for strong one-dimensional quantum confinement, resulting in anisotropic light emission. This characteristic of emission is mediated by the anisotropic TDMs which are dominantly in-plane for CQWs. During the formation of CQW films, controlling their assembly in face-down orientation, in which in-plane TDMs are parallel to the surface plane, provides directional emission profile, perpendicular to the surface plane of CQWs. Here, we demonstrate the liquid-interface self-assembly method to control orientation of these core/HIS CQWs film with entirely face-down and determine the exciton TDMs experimentally.

To achieve a single uniform monolayer face-down oriented CQWs, we precisely optimize the parameters of the liquid-interface self-assembly. Avoiding crack formation during the self-assembly process and defects on the surface are essential, since this directly affects the uniformity of orientation of the CQW film. Additionally, the concentration of CQWs in solution and indication of the solvent and subphases are significant factors of the formation of entirely uniform face-down orientation. During self-assembly process (see Figure 3.1), the substrates (quartz for optical measurement, and Si for microscopic images) are put in a Teflon well, and it is filled with acetonitrile (ACN) as the subphase. Afterward, 20 µL of CQWs in hexane solution of 15 mg/mL concentration is applied to the top of the subphase, and a waiting period is observed for the hexane to evaporate during the formation of a face-down oriented film of CQWs. Transition of the film to the substrate is provided with the drainage of the subphase.

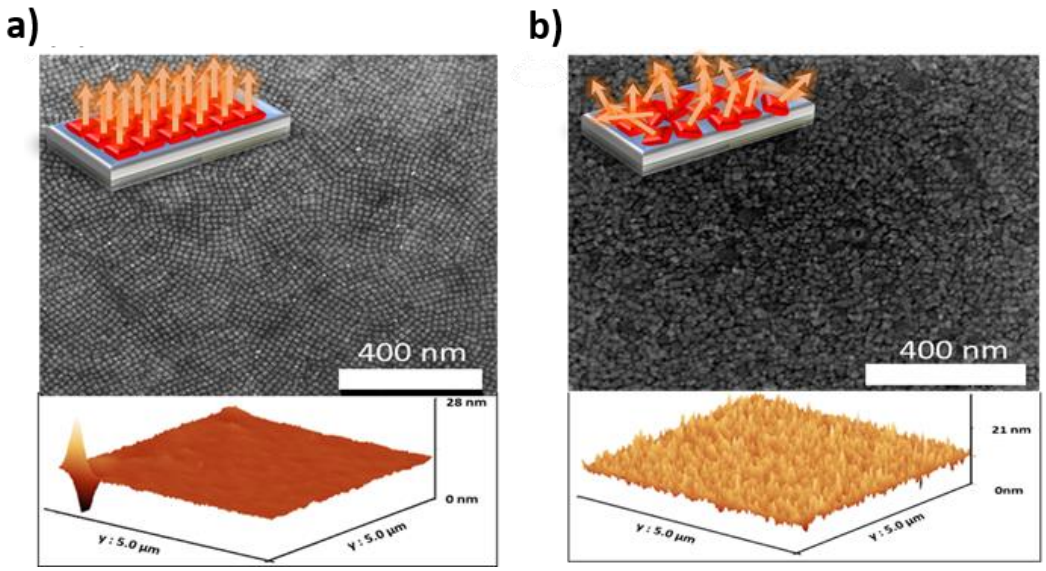

Figure 4. 2 Scanning electron microscopy (SEM) image of all-face-down oriented monolayer (a) and randomly-oriented spin-coated (b) CQW films with atomic force microscopy (AFM) measurements of them. Inset: Schematic diagrams of CQWs films with polarization of emission of self-assembled (a) and spin-coated (b).

The optimized self-assembly technique achieves uniform, entirely face-down oriented CQWs film with high surface coverage, as seen Figure 4.2a. Moreover, the resulting self-assembled film has smoother than 1 nm RMS roughness, while the value for the spin-coated film is 2.4 nm (see Figure 4.2b), resulting deficient morphological structure which affect the electrical properties of the light-emitting device.

Controlling the orientation of CQWs generates polarized light emission from their ensemble due to dielectric confinement effect and anisotropic distribution of TDMs. To confirm this presumption, we analyzed back focal plane (BFP) measurements (see Figures 3.7 and 3.8) of the face-down oriented and spin-coated CQW film on quartz substrates. The results of BFP measurements are shown in Figure 4.3. In the Fourier images, every point coincides with different emission angles, which are determined by the photon's wave vector and the orientation of the polarizer. Hence, the dipole orientation determines whether the emitted light becomes polarized in the s- or p- direction with respect to the polarizer.

As mentioned in scientific background, with the three-layer system (see Figure 2.15), interference and reflections of light, explained by Fresnel equations with the s- and p-polarizations, define local density of optical states (LDOS). The BFP image is defined by the LDOS and TDM orientations in the emissive layer.

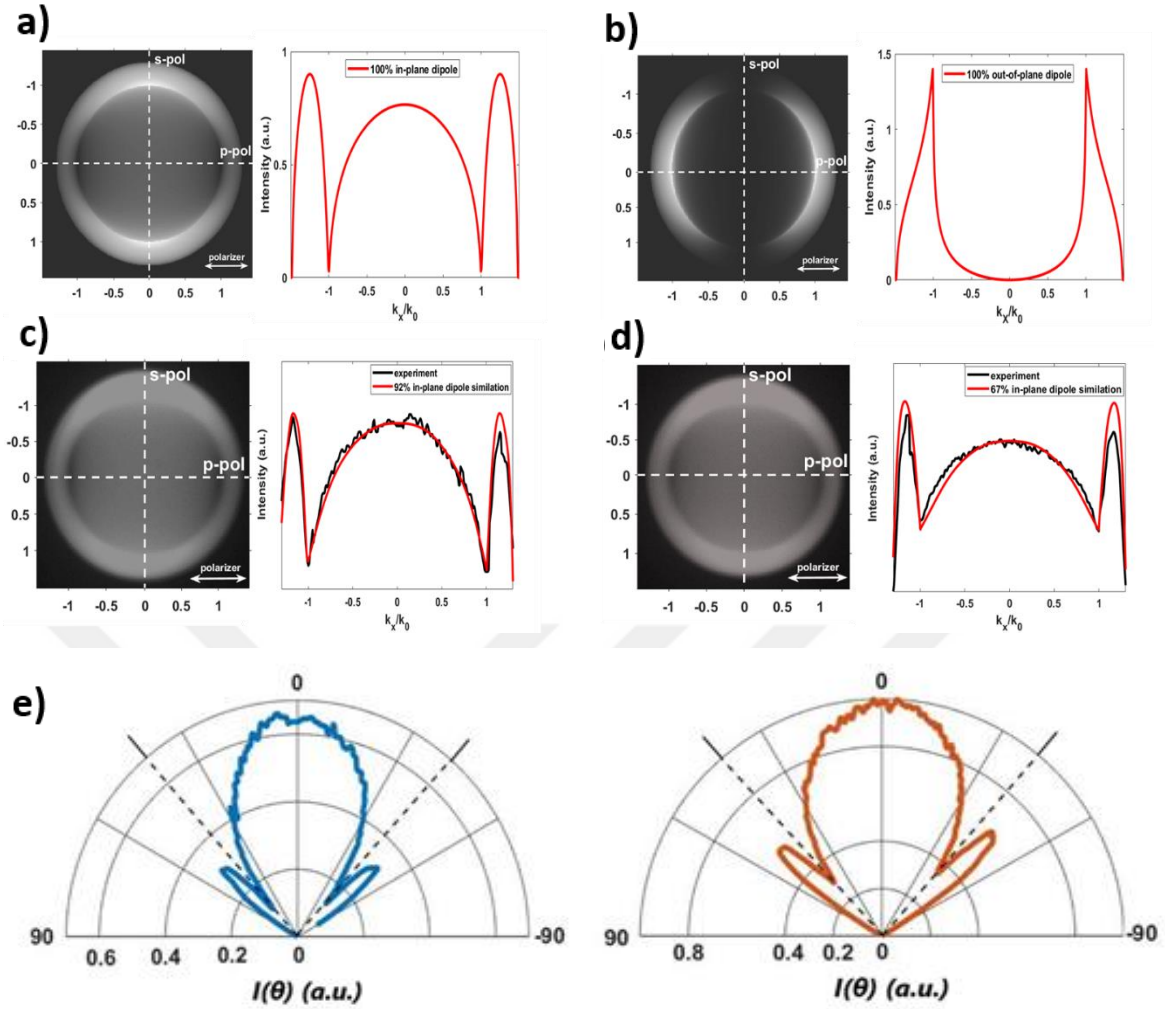

Figure 4. 3 BFP image patterns of the calculated emission profile and intensity diagrams of 100% in-plane TDMs (a) and 100% out-of-plane TDMs (b). Measured BFP image patterns and fitted k-space-dependent intensity profiles on the p-pol orientation of the face-down oriented self-assembly (c) and the spin-coated CQWs films (d). Corresponding polar intensity diagrams (e) of the face-down oriented self-assembly (blue), and the spin-coated (orange) CQWs films.

As shown in Figures 4.3a-b, the intensity spectra, obtained from the calculated BFP pattern, have no intensity for pure-in-plane TDMs at $k_x/k_0 = \pm 1$, and for the pure out-of-plane $k_x/k_0 = 0$. The fitting results, in Figures 4.3c and d, show that the ratio of the in-plane TDMs in the face-down oriented CQW film is 92% while it is 67% in the randomly-oriented spin-coated CQWs film, with a good agreement with the literature [42]. According to these results, the face-down orientation of CQWs leads to a higher contribution to the directed light emission through lateral surface plane with 4.1 times suppression of the out-of-plane TDMs distribution. However, although CQWs intrinsically have anisotropy due to the strong confinement in vertical thickness, their randomly-oriented films have random distribution of in-plane and out-of-plane TDMs located along the surface of a substrate.

Figure 4.3e shows the corresponding polar representation calculated according to the momentum profile of the face-down and the random oriented CQWs. The two side lobes define the emission modes at the angles beyond the total internal reflection (TIR) to the interface of the quartz-air at k_x/k_0 = 1. The pure in-plane TDMs have no emission at this angle, so the deeper line indicates the higher ratio of the in-plane TDMs, as we confirm with fitting lines.

In the light of these consequences, we fabricated a conventional structure of LED with the emissive layer consisting of all face-down orientation self-assembled monolayer of CQWs and as a reference we used spin-coated CQWs as the active emissive layer. As shown in Figure 4.4a-b, the structure of LEDs is composed of indium tin oxide (ITO, 100 nm)/poly(ethylene dioxythiophene):polystyrene sulphonate (PEDOT:PSS, 30 nm)/poly (N,N9-bis(4-butyl phenyl)-N,N9-bis(phenyl)-benzidine) (p-TPD, 20 nm)/ poly(9-vinyl carbazole) (PVK, 10 nm)/CQWs /Zn0.95Mg0.05O(30 nm) /Al (100 nm).

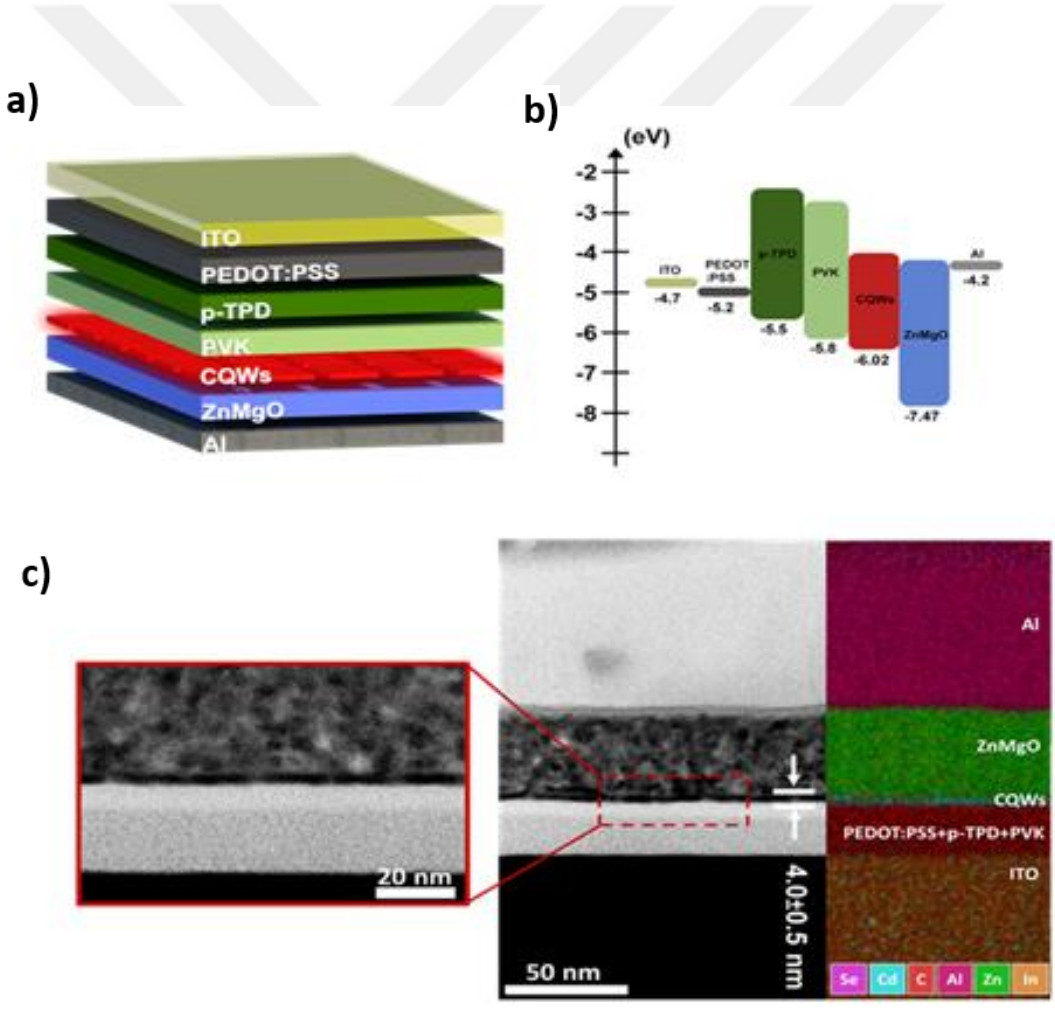

Figure 4. 4 Schematic illustration of device structure (a), energy level diagram (b), and cross-section image of our CQW-LEDs with the face-down oriented monolayer CQWs via transmission electron microscopy (TEM) along with energy-dispersive X-ray spectroscopy (EDAX) mapping (c).

As shown in Figure 4.4c, each layer in the LED structure, including the self-assembled monolayer (SAM) CQWs, is verified via cross-section profiled using EDAX. Here, the thickness of SAM CQWs, which is ~4.0±0.5 nm, is accurate given the actual thickness of core/HIS CQWs (see Figure 4.1). Therefore, the deposition of SAM film of CQWs is also successful in the LED structure. In the LED device, we benefited the deep highest-occupied-molecular-orbit (HOMO) energy level (5.8 eV) of PVK and the high hole mobility (10^{-4} $cm^{-1}V^{-1}s^{-1}$) of poly-TPD to obtain a stepwise energy level alignment between PEDOT:PSS and PVK as well as PVK and poly-TPD, and for the enhancement of hole injection. Additionally, to reduce the exciton quenching, we employed 5% Mg-doped ZnO as an electron transport layer (ETL). In Figure 4.5, the TEM image of ZnO nanoparticles is shown.

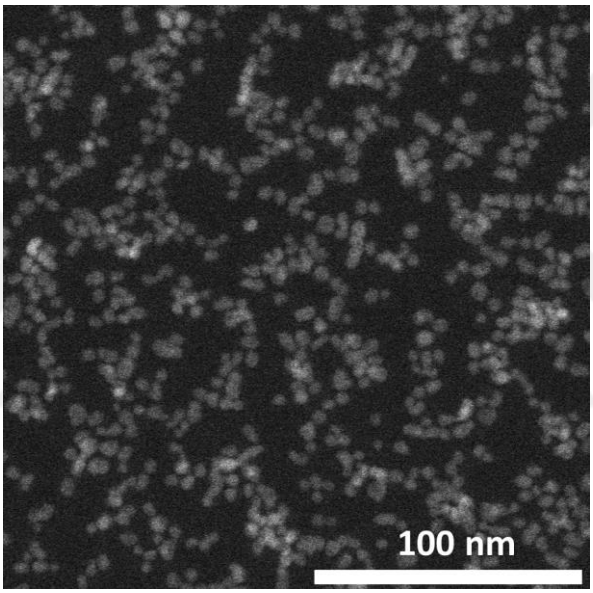

Figure 4. 5 TEM image of ZnMgO nanoparticles synthesized.

To understand the effect of directed emission resulting from the face-down oriented film of CQWs on the light outcoupling efficiency considering the structure of LEDs, according to the ratio of the in-plane and out-of-plane TDMs, we calculated the light outcoupling efficiency by finite-discrete time-domain (FDTD) method (see Figure 4.6).

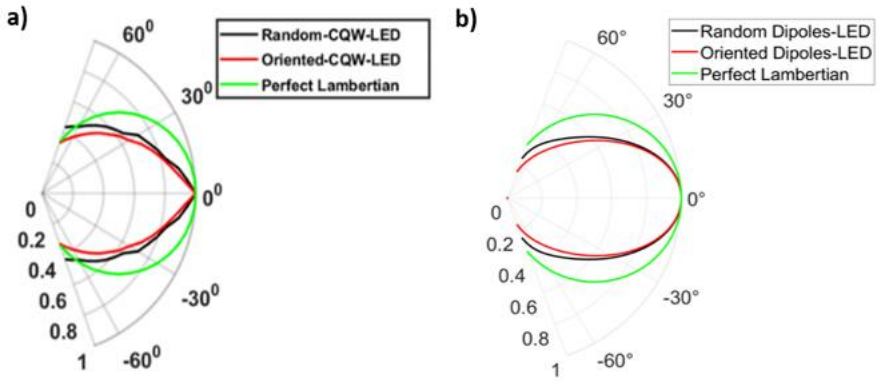

Figure 4. 6 Angular distribution of extracted light emission from LEDs with the emissive layer of the oriented and random CQWs, experimentally measured (a) and numerically calculated (b).

As shown in Figure 4.6, the angular distribution of the emission of LEDs with the electroluminescent layer of face-down oriented CQWs is narrower than those of both randomly-oriented CQWs-LEDs and perfect Lambertian emission profiles, with a good agreement of the measured and calculated profiles. According to the calculations, the outcoupling efficiency, based on 92% in-plane TDMs ratio of face-down oriented CQWs, is predicted to be 34%, if the light is outcoupled from the top while for 67% in-plane TDMs ratio of spin-coated CQWs, this is 22%, supporting a significant improvement of 54.5%. The multilayered structure of LED that including various materials with different refractive indices, results in reflected and refracted of light at interfaces, creating partial waveguiding effect within lateral structure. This effect is the reason of a narrower profile of the randomly-oriented CQW-LEDs than expected, since it causes restriction on the emission angle of light within a narrow light-extraction cone.

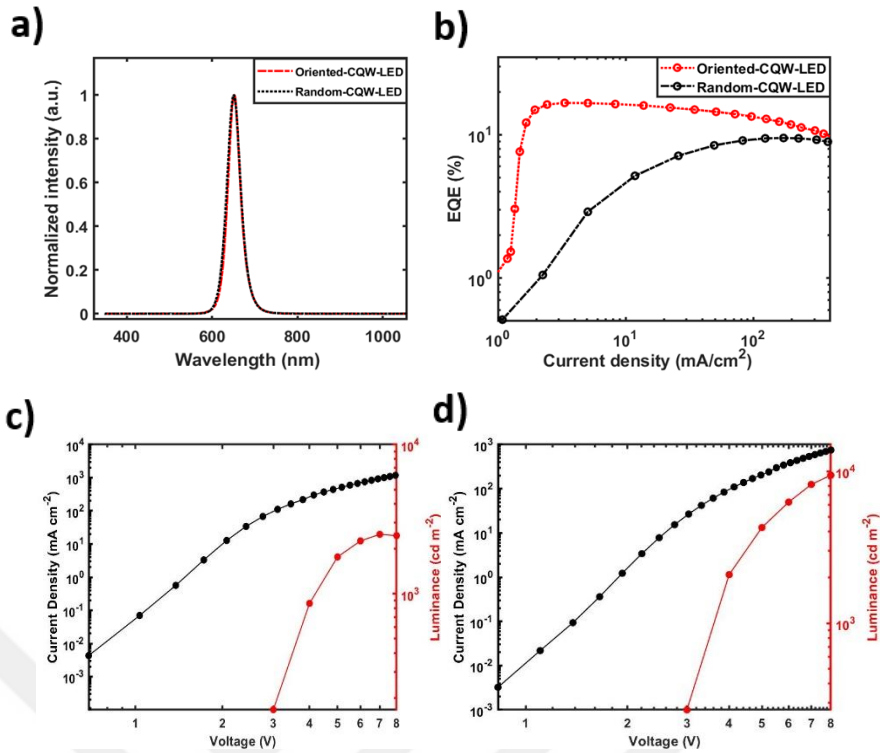

Figure 4. 7 Normalized electroluminescence (EL) intensity spectrum (a), and EQE versus current density (b) of the face-down oriented-CQW-LED and the random-oriented CQW-LED devices. Current density versus voltage of the random-oriented CQW-LED (c) and the face-down oriented-CQW-LED (d).

EL spectra of the devices fabricated using two different methods, one involving precise orientation through the self-assembly (face-down oriented CQW-LED) and the other involving random orientation through spin-coating (random-CQW-LED), exhibit identical peaks at 650 nm, exactly the same for both of them (see Figure 4.7a). As seen in Figure 4.7b, the efficiency measurements provide EQE values of 16.3% for the oriented-CQW-LED and 9.5% for the random-CQW-LED. A direct comparison between the two devices reveals a substantial 71.5% increase in EQE. Moreover, comparison of the luminance values from these two types of LED devices indicates increased brightness with the emissive layer of the face-down oriented CQWs (see Figure 4.7c-d). Our analysis attributes 54.5% of this improvement to the enhanced light outcoupling along with improved charge injection and reduced reabsorption, which together enable high EQE values at a lower current density, particularly when utilizing a face-down oriented single monolayer of CQWs.

4.2. All-Edge-Up Oriented Colloidal Quantum Well Based Light-Emitting Diodes

4.2.1. Control Mechanism of Edge-up Orientation Self-assembly of CQWs

To obtain pin-hole free edge-up oriented CQWs film, we need to control three main different factors, the subphase as the liquid medium, the solvents and the concentration of CQWs. Understanding the effects of these factors individually, we need to change only one parameter while the others are taken as a reference. Therefore, we started our experiments by optimizing the subphase, directly relying on the polarity difference to create strong repulsive forces between CQWs.

Acetonitrile, diethylene glycol, and ethylene glycol are generally used as the subphase for the self-assembled films of NCs. The main criteria of selecting subphase is based on the polarity difference with respect to the solvents of NCs. We performed a set of experiments using three types of liquids as the subphase, while the hexane is used for the solvent of our CQWs of CdSe/CdZnS core/HIS at 15 mg/mL concentration at room temperature. As mentioned in experimental methods, we used a 5 cm radius Teflon well housing a hole to allow for the drainage of the subphase by a syringe (see Figure 3.1). For all types of the subphase, we filled Teflon well with 20 mL subphase, which is the minimum required volume to expedite their evaporation after the self-assembly process. To reduce the solvent's rate of evaporation after the addition of the CQWs dispersion, the Teflon well was covered with a glass petri dish. The petri dish was removed after 40 min to allow the solvent to completely evaporate. Then, the subphase was carefully removed by a syringe after waiting further for 20 min to allow the produced film to be deposited on the desired substrate. In Figure 4.8, SEM images of the self-assembled films obtained from this process are shown.

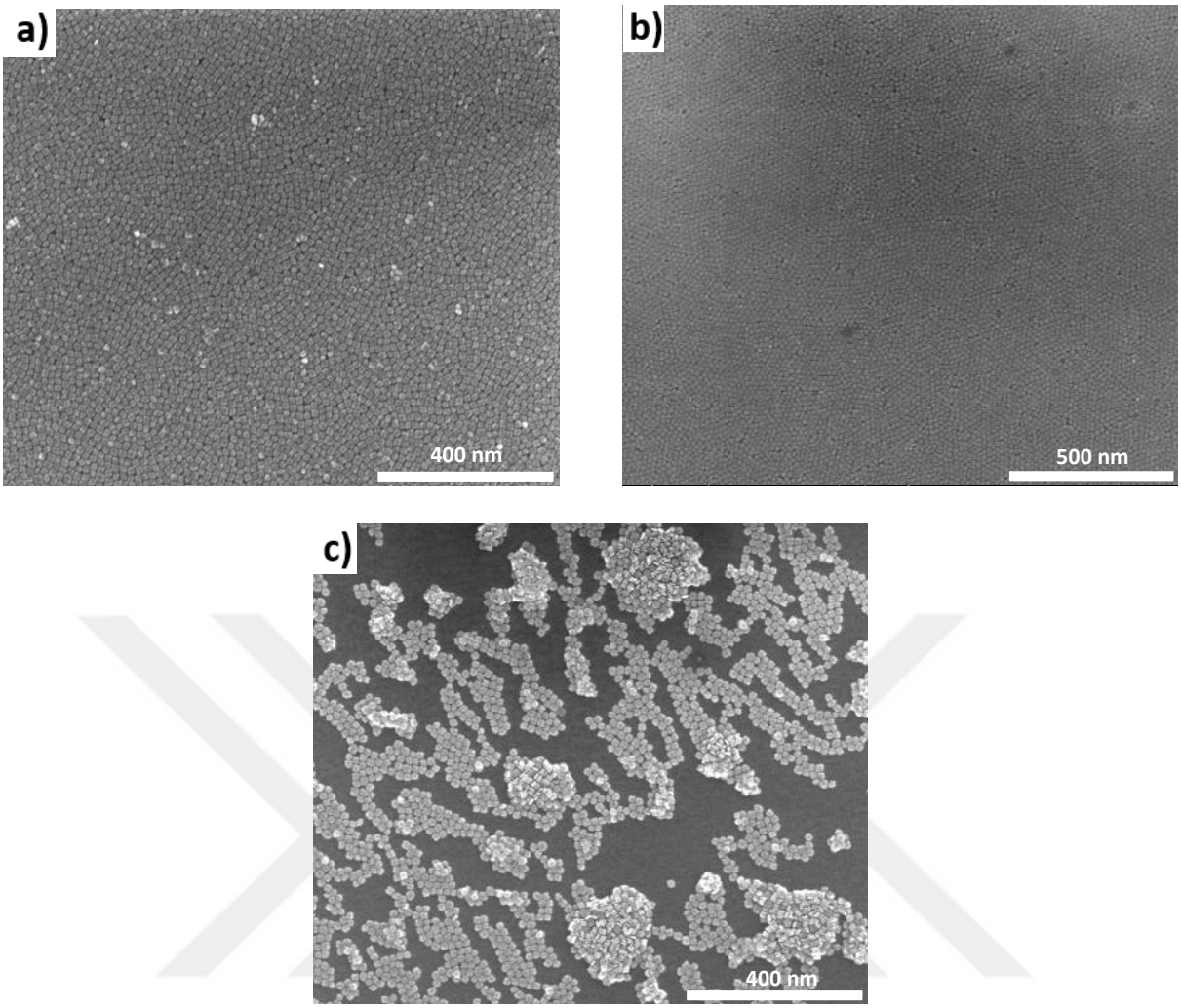

Figure 4. 8 SEM images of the self-assembled films of CdSe/CdZnS core/HIS CQWs on Si substrates. The solvent of CQWs is hexane, and the subphase is acetonitrile (a), diethylene glycol (b), and ethylene glycol (c). Note that, for each set, the concentration of CQW solution is 15 mg/mL and the amount of dropping is 20 μL.

As shown in Figure 4.8c, although the tendency of edge-up oriented CQWs appears more likely with ethylene glycol subphase, we cannot conclude that it is optimized, since using hexane as the solvent and 20 mg/mL concentration are not appropriate for the edge-up oriented film.

Based on the previous set of experiments, while we used ethylene glycol as the subphase, we changed the types of solvents from hexane to heptane and octane. The main difference between these solvents are the evaporation rate, 0.103 $\mu L/s \cdot cm^2$ for hexane, 0.023 $\mu L/s \cdot cm^2$ for heptane, and 0.018 $\mu L/s \cdot cm^2$ for octane. The CQWs need adequate time to stack up. Thus, rapid evaporation means that development of the edge-up configuration cannot have completed. As seen in Figure 4.9, octane provides a sufficiently slow evaporation rate to give enough time for the edge-up oriented CQWs. The

orientation of CQWs exhibits a trend from the face-down to the edge-up by changing the solvents from hexane to heptane, and finally to octane.

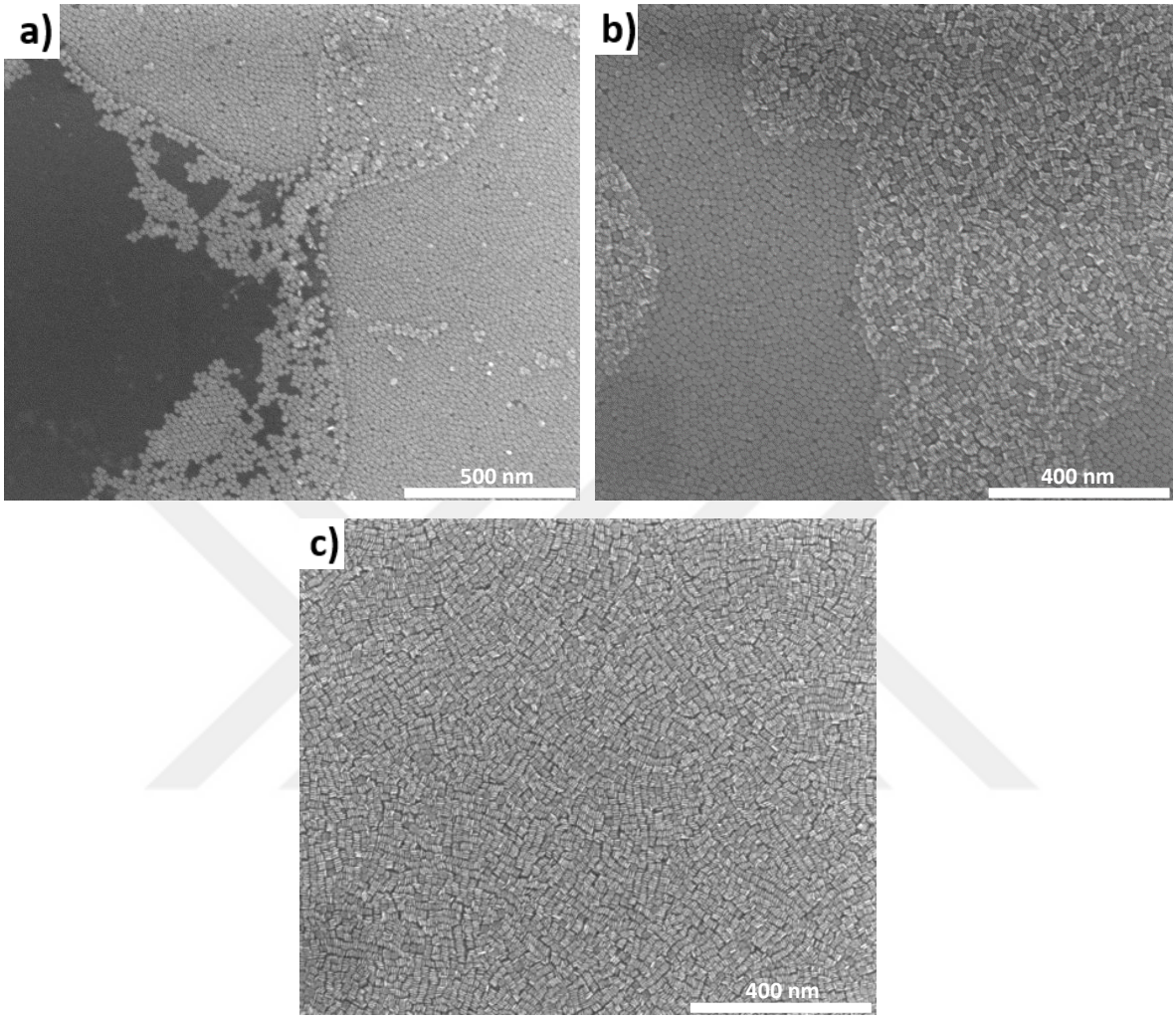

Figure 4. 9 SEM images of the self-assembled film of our CdSe/CdZnS core/HIS CQWs on Si substrates. The subphase is ethylene glycol, and the solvents are hexane (a), heptane (b), and octane (c). Note that, for each set, the concentration of CQWs solution is 15 mg/mL and the amount of dropping is 20 μL.

With the subphase of ethylene glycol and the solvent of octane, the edge-up oriented self-assembly of CQWs has been successful. However, for the surface coverage, especially across a large area, we need to optimize the concentrations of CQWs solution. For coverage of a piece of Si substrate with dimension of 1×1 cm^2, we carried on a set of experiments with various concentrations. We found that lower concentrations of CQWs dissolved in the octane cause the formation of cavities on the surface, while high concentrations cause overlapping of CQWs. As shown in Figure 4.10, the optimal concentration for a full surface coverage is 20 mg/mL.

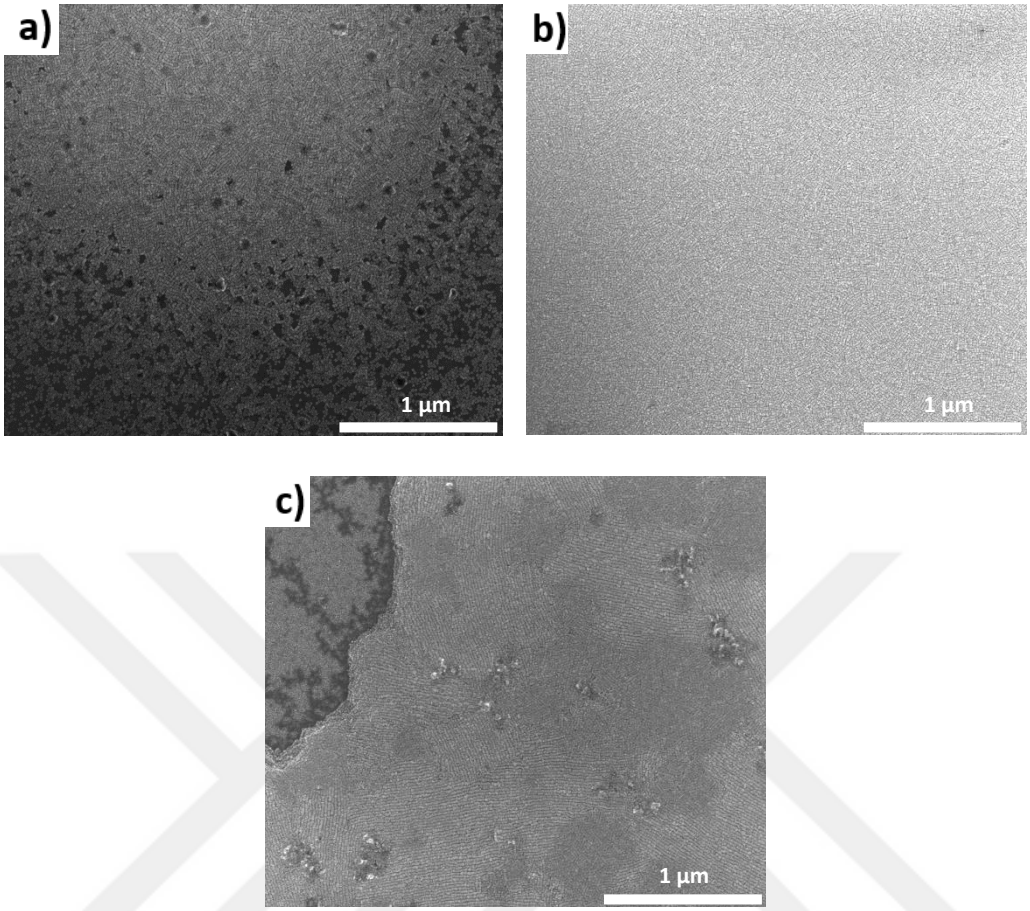

Figure 4. 10 SEM images of the edge-up self-assembled film of our CdSe/CdZnS core/HIS CQWs on Si. The subphase is ethylene glycol, and the solvent is octane with concentrations of 10 mg/mL (a), 20 mg/mL (b), and 30 mg/mL (c).

When various concentrations of CQWs in octane at 10, 20, and 30 mg/mL are used for the formation of edge-up oriented self-assembly film, main differences are observed on the morphological properties of representing films. We also discovered that concentration values affect the length of chain formation of the edge-up oriented CQWs. In this set of experiments, we used 20, 24, and 26 mg/mL concentrations without changing other parameters of the subphase and while keeping the dropping amount of CQWs solution (20 µL) and the temperature of environment (the room temperature fixed). Figure 4.11 shows three different lengths of chain formation of the edge-up orientation of CQWs, and the average number of CQWs is 47.7 in the long chain, 26.3 in the middle chain, and 12.9 in the short chain, calculated by ImageJ.

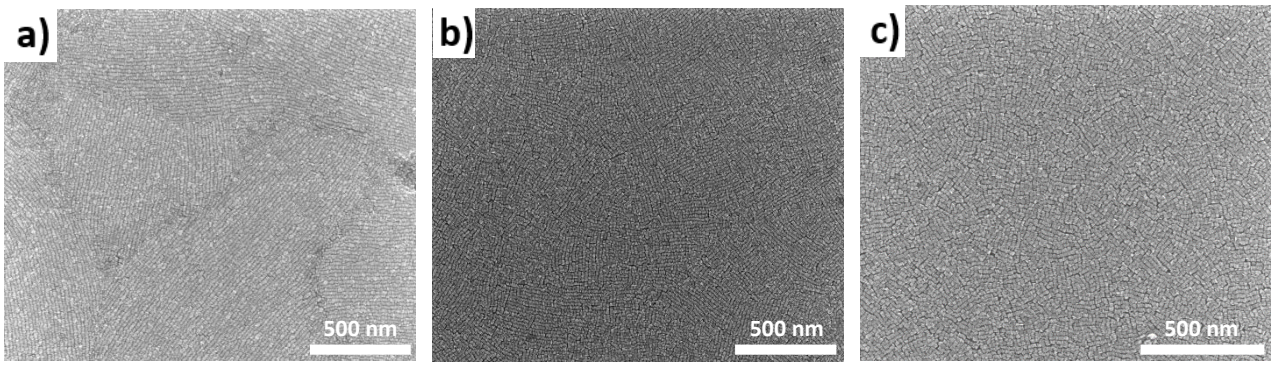

Figure 4. 11 SEM images of the edge-up self-assembled films of our CdSe/CdZnS core/HIS CQWs on Si. The subphase is ethylene glycol, and the solvent is octane with concentrations of 26 mg/mL for the long chain (a), 24 mg/mL for the middle chain (b), and 20 mg/mL for the short chain (c).

We analyzed the Fouier-plane images of single particle CQW and edge-up oriented self-assembly films of CQWs with short and long chains. Single particle CQW obtained with spin-coating CQW solution with 1000× times diluted. According to the BFP measurements, while out-of-plane TDMs were not resolved for the single particle CQWs long-chained edge-up oriented CQWs exhibited 3.5 times more out-of-plane TDMs contribution than that of the short-chained edge-up oriented CQWs.

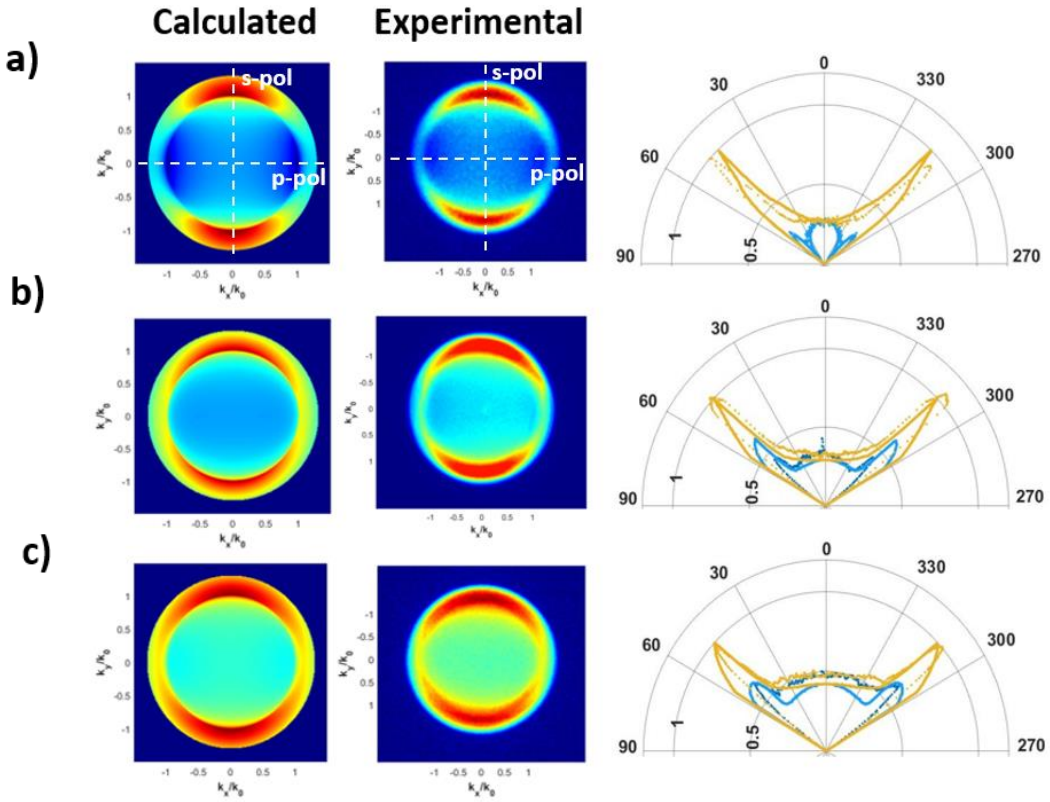

Figure 4. 12 Numerically calculated and experimentally measured BFP images, and the polar plots of a single particle (a), short-chained (b) and long-chained (c) edge-up oriented CQWs.

In Figure 4.12, the experimental and calculated BFP images, along with polar plots of single-particle, short-chained, and long-chained edge-up oriented CQWs films are presented. The radius in the plots are maximum angle at which the collected emission coming from objective depends on N.A. (N.A.=1.3), $\theta_{coll} = \sin^{-1}(N.A./n_{quartz})$. The radiation patterns are fitted by the sum of three dipoles stronger or weaker in-plane, or out-of-dipole, represented by coefficients $\eta_{II,1}$, $\eta_{II,2}$, and $\eta_{\perp}$, respectively. The coefficient is taken proportional to the square of its dipole moments and then they normalized. As in seen in Figure 4.12, the fitted curves in polar plots have an excellent agreement with the experimental curves. According to the results here, while the contribution of dipoles is for the single-particle CQW such that

$$\eta_{II,1} = 0.68, \eta_{II,2} = 0.32, \eta_{\perp} = 0,$$

for the short-chained edge-up oriented CQWs, we have

$$\eta_{II,1} = 0.6, \eta_{II,2} = 0.3, \eta_{\perp} = 0.1,$$

for the long-chained edge-up oriented CQWs, this is

$$\eta_{II,1} = 0.45, \eta_{II,2} = 0.2, \eta_{\perp} = 0.35,$$

The striking difference on the contributions of three TDMs between the samples is that CQWs exhibit only in-plane TDMs, while this is not the case for self-assembled films as also reported by others authors [62].

4.2.2. Long-Chained and Short-Chained Edge-Up Oriented Colloidal Quantum Well Based Light-Emitting Diodes

In this part of the thesis work, we demonstrated inverted-structure light-emitting diodes with the emissive layers of long-chained and short-chained edge-up oriented CdSe/$Cd_{0.25}Zn_{0.75}S$ core/HIS CQWs. Optimizations on the LED structure were conducted to achieve high current efficiency with all-edge-up oriented self-assembled CQW EML. Following these our optimizations, EMLs with the face-down oriented and spin-coated CQWs are used as reference during our experiments.

The structure of LEDs studied in this part is inverted, and as mentioned before, we started with cleaning processes of our substrates with Hellmanex detergent dissolved in deionized water, acetone, and isopropanol bath. The deposition of all other layers is carried out in N_2 filled glovebox system. As ETL and EIL, we used 40 nm thick ZnO nanoparticle film deposited spin-coated on ITO-coated substrates. Then, the spin-coated and self-assembled EMLs are deposited on the ZnO layer. The spin-

coated EML is annealed on hot plate at 80 ^{0}C for 10 min, and self-assembled EML is kept in a vacuum system in glove box for evaporation of the solvent. As the hole transporting and hole injection layers, we used CBP and MoO_3 with 60 and 10 nm thicknesses, respectively. Finally, 100 nm thick Al layer is thermally evaporated as the anode of the LED. Figure 4.13a demonstrates the schematic diagram of CQW-LED structure. This device architecture provides a stepwise energy band alignment to ease the charge injection (see Figure 4.13b).

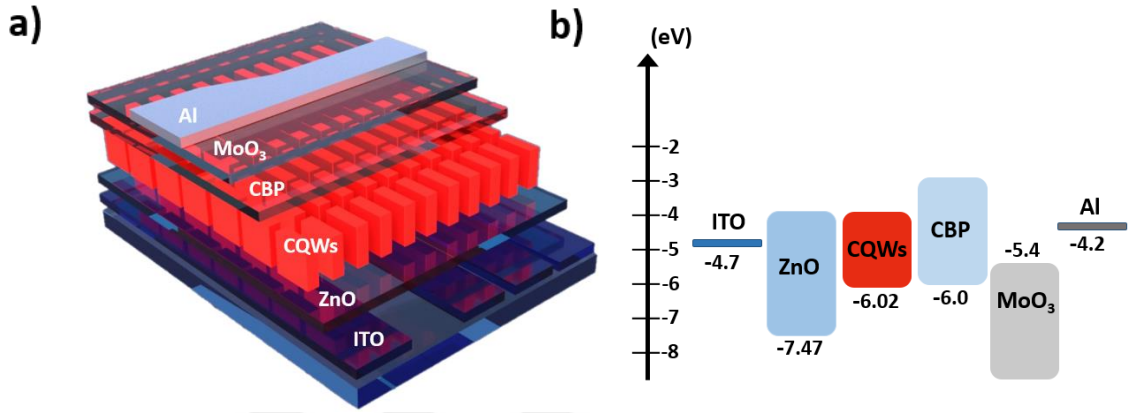

Figure 4. 13 Schematic illustration of the structure (a) and energy level diagram of LEDs (b) we fabricated.

After the encapsulation of LEDs, for the electrical and optical characterizations, LEDs are taken into air environment. First, we measured the EL spectra of the spin-coated, face-down, and edge-up orientated self-assembled CQW LEDs (see Figure 4.14). For all configurations of EML, the emission intensity peak is found at 648 nm with FWHM of 35 nm.

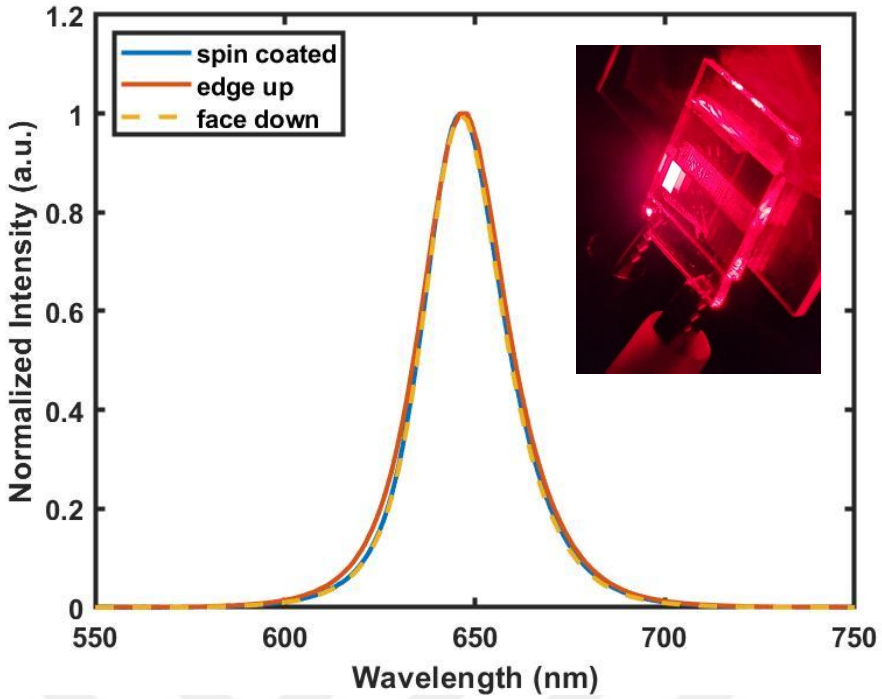

Figure 4. 14 EL spectra of our LED with the spin-coated, face-down, and edge-up oriented CQW EML. Inset: photograph of the LED with edge-up oriented CQW EML driven at 7 V.

For other electrical and optical characterizations, the LED samples are putted into an integrated sphere system and to measure the luminance values, we used a spectroradiometer as mentioned in the experimental method part. In Figure 4.15, EQE, J-V, and L-V graphs of our LEDs with long-chained and short-chained edge-up oriented CQWs with the control groups of the face-down oriented and spin-coated CQWs used as the EML are shown. As seen in the figure, with long-chained edge-up oriented CQWs as the EML, LEDs exhibit a stronger luminance value of 4000 cd/m^2 improved more than 50% compared to short-chained edge-up oriented CQW-LED. The device efficiency enhances from 12.5% to 17.5%.

Moreover, regardless of the chain length of the edge-up oriented CQWs, the charge injection efficiency is increased by 60%, as seen in Figure 4.15. To prove that, we also constructed electron-only devices whose structure is ITO (100 nm)/ZnO (40 nm)/CQWs/Al (100 nm). CQWs in this device are deposited into the same configuration as the actual LEDs (see Figure 4.16).

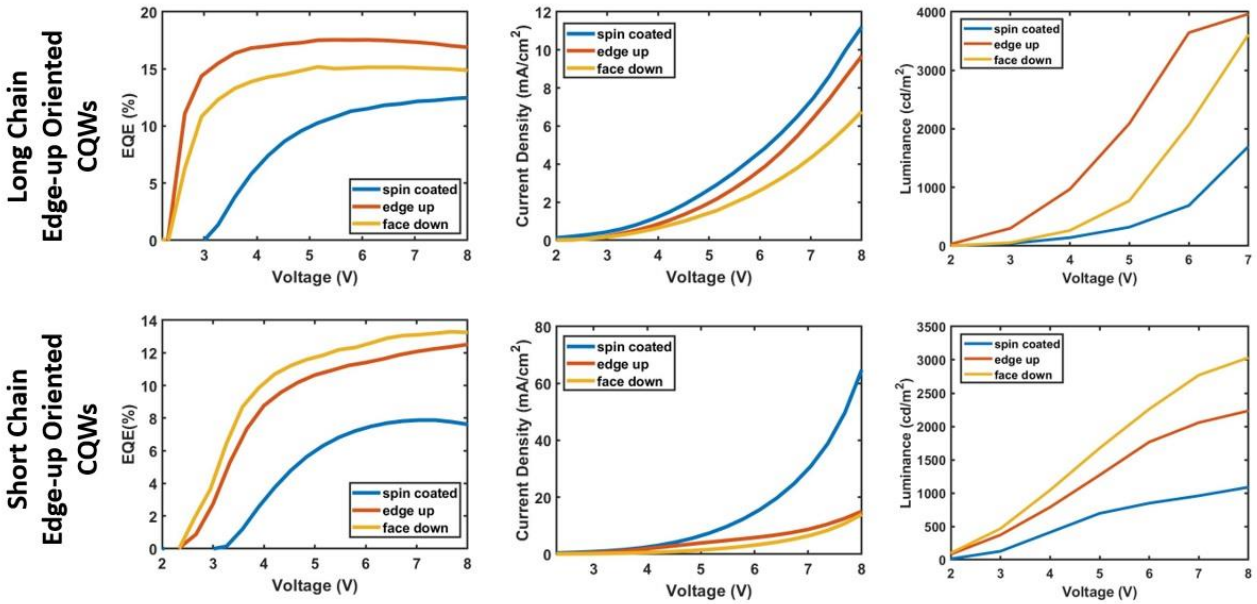

Figure 4. 15 EQE vs. voltage, current density vs. voltage, and luminance level of LEDs using EMLs of the long-chained and short-chained edge-up oriented CQWs with the control groups of face-down oriented and spin-coated CQWs.

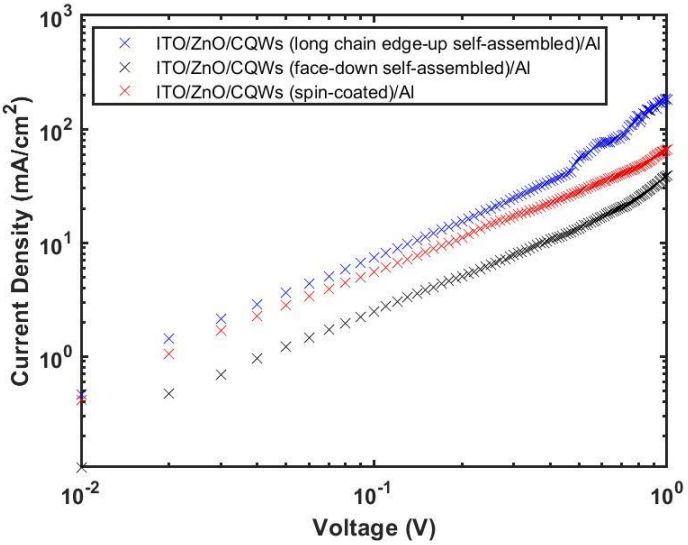

Figure 4. 16 Current density vs. voltage graph of the electron-only devices using different configurations of CQWs.

The other main parameter affecting the efficiency performance of CQW-LEDs is the surface quality of layer. To understand this property, we performed AFM measurements for all deposited layers used in the inverted-structure of LEDs (see Figure 4.17). Given the roughness level of each layer, the edge-up oriented CQWs on ZnO yields quite low RMS roughness value of 1.21 nm, with the thermally evaporated layers of CBP and MoO_3 being extremely smooth.

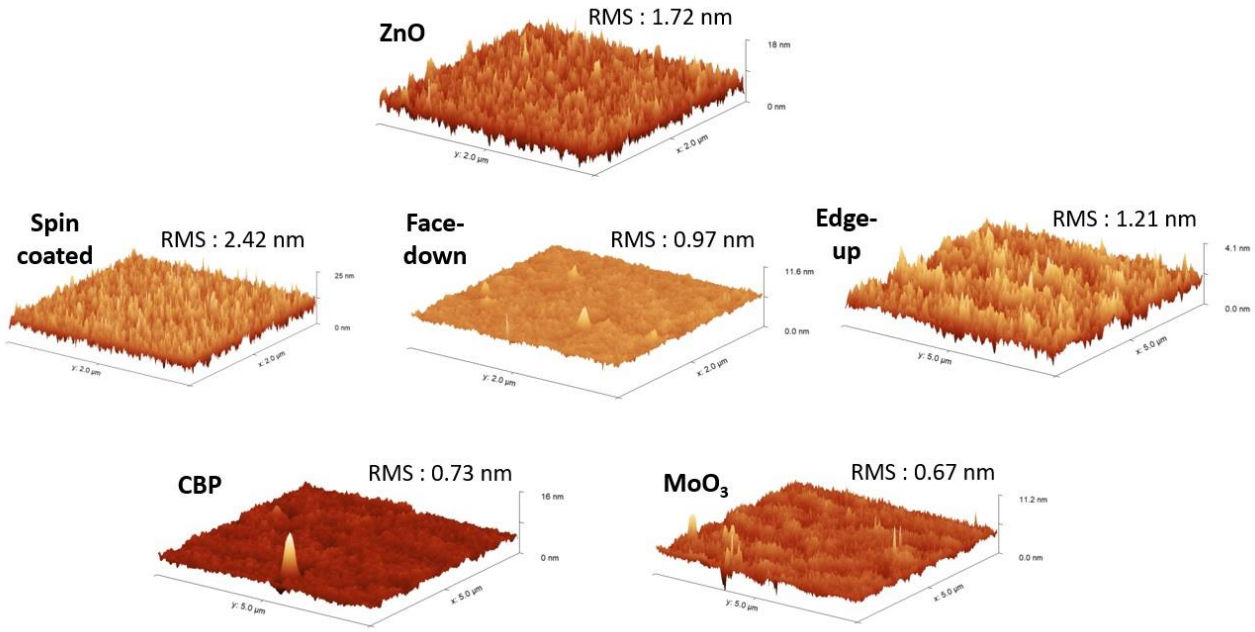

Figure 4. 17 Atomic force microscopy (AFM) results of the device layers used in the structure of our LEDs.

4.3. Summary

The EL spectra of the devices constructed using two different methods, one involving precise orientation through the self-assembly (oriented-CQW-LED) and the other involving random orientation through the spin-casting (random-CQW-LED), exhibit the identical emission peaks at 650 nm without any noticeable spectral shift. BFP measurements of the CQWs show that the CQWs have intrinsically anisotropic TDMs dominant in the plane orientation. However, randomly-oriented CQW films cannot exhibit directed light emission, since the total distribution of in-plane TDMs through the film dramatically decreases. The controlling of face-down orientation of CQWs allow to contribute more directed emission from the CQW film. The peak EQE value is 16.3% for the oriented-CQW-LED and 9.5% for the random-CQW-LED. A direct comparison between the two devices reveals a substantial 71.5% increase in the EQE. Our analysis attributes this 54.5% improvement to the enhanced light outcoupling, while the remaining 17% can be attributed to the improved charge injection and reduced reabsorption, particularly when utilizing a single ordered monolayer of CQWs. Furthermore, the NPL film oriented with all-face-down configuration exhibits the least surface roughness compared to alternative deposition techniques, thereby possibly improving charge injection.

Also, we demonstrated edge-up oriented self-assembly of CQWs used for the first time in an inverted LED with the emissive layer of edge-up oriented CdSe/$Cd_{0.25}Zn_{0.75}S$ core/HIS CQWs. The optimized edge-up self-assembly CQWs in liquid-interface enables high surface coverage over a large area, and concentrations of CQW solution in octane used for the self-assembly generates different chain lengths of the edge-up orientation self-assembly. Fourier plane analysis of single-particle, short-chained, and long-chained edge-up oriented CQWs shows that the out-of-plane transition dipole moments cannot resolved for single-particle CQWs, while the ratio of out-of-plane transition dipole moments is 10% for the short-chain, and 35% for the long-chain edge-up oriented CQWs. Moreover, using the edge-up oriented CQWs in electron-only devices, current-density dependent voltage analysis shows improvement current injection efficiency. The use of such short- and long-chained edge-up oriented CQWs in LED enables an enhancement of 40% in the EQE, and of more than 50% in brightness. These findings show that the suggested edge-up oriented-CQW LED design can be used to create high-performance CQW-LEDs.

CHAPTER 5

5 Conclusion and Future Outlook

In this thesis, first, we have successful fabricated conventional-structure CQW-LED using all-face-down oriented self-assembly method. The face-down oriented CQWs as the emissive layer provides a highly uniform film, with a low roughness value and free of pin-hole which contribute to efficient charge injection. The most significant optical property of CQWs is the direction-dependent emission unlike quantum dots. This property provides strong in-plane transition dipole moment contribution in the face-down oriented CQWs with a 92% ratio, much higher than that of conventional spin-coated film. High directional emission gives rise to improvement in the outcoupling efficiency. As a result, we attained high external quantum efficiency of 18.1% with a peak luminance value of 19,800 cd/m^2, corresponding to 65% advancement in comparison to the performance of LED with randomly-oriented CQWs as the emissive layer.

The second study included in this thesis focuses on all-edge-up oriented CQWs used as the emissive layer of inverted-structure LEDs. First, we showed the most efficient method to obtain uniform edge-up oriented film and then we worked in detail for obtaining longer chain lengths of CQWs on film. Longer chain provides a stronger out-of-plane transition dipole moment contribution. Therefore, higher percent of directional emission is achieved. Also, improvement in the charge injection efficiency originating from edge-up oriented CQWs makes them highly promising for CQW-LEDs. Second, we fabricated evaporation-based LEDs with edge-up oriented CQW as the emissive layer. Results show that longer chain edge-up oriented CQW film ensured luminance and EQE values enhanced by 40% and 50% times, respectively.

Despite all the achievements shown in this thesis, further future works are required to develop a deep understanding of the reasons and saturation points of stronger out-of-plane transition dipole moments in the longer chain edge-up orientated self-assembled film of CQWs. Additionally, to develop both optical and electrical properties of CQWs, different constructions of the oriented films in LED devices can be examined. Also, the fabrication parameters can be further optimized for the systematic variation and selection of the charge injection and transport layers to reach maximum EQE and luminance values.

Bibliography

[1] Shur, M., & Zukauskas, R. (2005, October). Solid-State Lighting: Toward Superior Illumination. Proceedings of the IEEE, 93(10), 1691–1703. https://doi.org/10.1109/jproc.2005.853537

[2] Song, X., Chang, M. H., & Pecht, M. (2013, August 29). Rare-Earth Elements in Lighting and Optical Applications and Their Recycling. JOM, 65(10), 1276–1282. https://doi.org/10.1007/s11837-013-0737-6

[3] Baldo, M. A., O'Brien, D. F., You, Y., Shoustikov, A., Sibley, S., Thompson, M. E., & Forrest, S. R. (1998, September). Highly efficient phosphorescent emission from organic electroluminescent devices. Nature, 395(6698), 151–154. https://doi.org/10.1038/25954

[4] Ronda, C., Jüstel, T., & Nikol, H. (1998, July). Rare earth phosphors: fundamentals and applications. Journal of Alloys and Compounds, 275–277, 669–676. https://doi.org/10.1016/s0925-8388(98)00416-2

[5] Liu, B., Altintas, Y., Wang, L., Shendre, S., Sharma, M., Sun, H., Mutlugun, E., & Demir, H. V. (2019, December 23). Record High External Quantum Efficiency of 19.2% Achieved in Light-Emitting Diodes of Colloidal Quantum Wells Enabled by Hot-Injection Shell Growth. Advanced Materials, 32(8), 1905824. https://doi.org/10.1002/adma.201905824

[6] Moon, H., Lee, C., Lee, W., Kim, J., & Chae, H. (2019, January 16). Stability of Quantum Dots, Quantum Dot Films, and Quantum Dot Light-Emitting Diodes for Display Applications. Advanced Materials, 31(34), 1804294. https://doi.org/10.1002/adma.201804294

[7] A. Fakharuddin et al., "Perovskite light-emitting diodes," Nat Electron, vol. 5, no. 4, pp. 203–216, 2022.

[8] Bourget, C. M. (2008, December). An Introduction to Light-emitting Diodes. HortScience, 43(7), 1944–1946. https://doi.org/10.21273/hortsci.43.7.1944

[9] Erdem, O., & Demir, H. V. (2022). Self-Assembly of Colloidal Nanocrystals. Oriented Self-Assembly of Colloidal Semiconductor Nanoplatelets on Liquid Interfaces, 15–27. https://doi.org/10.1007/978-981-19-7052-8_3

[10] Maserati, L., Refaely-Abramson, S., Kastl, C., Chen, C. T., Borys, N. J., Eisler, C. N., Collins, M. S., Smidt, T. E., Barnard, E. S., Strasbourg, M., Schriber, E. A., Shevitski, B., Yao, K., Hohman, J. N., Schuck, P. J., Aloni, S., Neaton, J. B., & Schwartzberg, A. M. (2021). Anisotropic 2D excitons

unveiled in organic–inorganic quantum wells. Materials Horizons, 8(1), 197–208. https://doi.org/10.1039/c9mh01917k

[11] Schuller, J. A., Karaveli, S., Schiros, T., He, K., Yang, S., Kymissis, I., Shan, J., & Zia, R. (2013). Orientation of luminescent excitons in layered nanomaterials. Nature Nanotechnology, 8(4), 271–276. https://doi.org/10.1038/nnano.2013.20

[12] Murray, C. B., Norris, D. J., & Bawendi, M. G. (1993, September). Synthesis and characterization of nearly monodisperse CdE (E = sulfur, selenium, tellurium) semiconductor nanocrystallites. Journal of the American Chemical Society, 115(19), 8706–8715. https://doi.org/10.1021/ja00072a025

[13] Polavarapu, L., Nickel, B., Feldmann, J., & Urban, A. S. (2017). Advances in Quantum-Confined Perovskite Nanocrystals for Optoelectronics. Advanced Energy Materials, 7(16). https://doi.org/10.1002/aenm.201700267

[14] A.I. Ekimov, Al.L. Efros, M.G. Ivanov, A.A. Onushchenko, S.K. Shumilov, Donor-like exciton in zero-dimension semiconductor structures, Solid State Communications, Volume 69, Issue 5, 1989, Pages 565-568, ISSN 0038-1098, https://doi.org/10.1016/0038-1098(89)90242-1.

[15] Kambhampati, P. (2021, May 13). Nanoparticles, Nanocrystals, and Quantum Dots: What are the Implications of Size in Colloidal Nanoscale Materials? The Journal of Physical Chemistry Letters, 12(20), 4769–4779. https://doi.org/10.1021/acs.jpclett.1c00754

[16] Pelekanos, N. T., Ding, J., Hagerott, M., Nurmikko, A. V., Luo, H., Samarth, N., & Furdyna, J. K. (1992, March 15). Quasi-two-dimensional excitons in (Zn,Cd)Se/ZnSe quantum wells: Reduced exciton–LO-phonon coupling due to confinement effects. Physical Review B, 45(11), 6037–6042. https://doi.org/10.1103/physrevb.45.6037

[17] Ramalingam, G., Kathirgamanathan, P., Ravi, G., Elangovan, T., Arjun kumar, B., Manivannan, N., & Kasinathan, K. (2020, June 24). Quantum Confinement Effect of 2D Nanomaterials. Quantum Dots - Fundamental and Applications. https://doi.org/10.5772/intechopen.90140

[18] Diroll, B. T., Greybush, N. J., Kagan, C. R., & Murray, C. B. (2015, April 8). Smectic Nanorod Superlattices Assembled on Liquid Subphases: Structure, Orientation, Defects, and Optical Polarization. Chemistry of Materials, 27(8), 2998–3008. https://doi.org/10.1021/acs.chemmater.5b00355

[19] Chen, Z., Nadal, B., Mahler, B., Aubin, H., & Dubertret, B. (2013, July 16). Quasi-2D Colloidal Semiconductor Nanoplatelets for Narrow Electroluminescence. Advanced Functional Materials, 24(3), 295–302. https://doi.org/10.1002/adfm.201301711

[20] Ithurria, S., Tessier, M. D., Mahler, B., Lobo, R. P. S. M., Dubertret, B., & Efros, A. L. (2011, October 23). Colloidal nanoplatelets with two-dimensional electronic structure. Nature Materials, 10(12), 936–941. https://doi.org/10.1038/nmat3145

[21] Ithurria, S., & Dubertret, B. (2008). Quasi 2D colloidal CdSe platelets with thicknesses controlled at the atomic level. Journal of the American Chemical Society, 130(49), 16504–16505. https://doi.org/10.1021/ja807724e

[22] Kelestemur, Y., Olutas, M., Delikanli, S., Guzelturk, B., Akgul, M. Z., & Demir, H. V. (2015, January 17). Type-II Colloidal Quantum Wells: CdSe/CdTe Core/Crown Heteronanoplatelets. The Journal of Physical Chemistry C, 119(4), 2177–2185. https://doi.org/10.1021/jp510466k

[23] TUGOLUKOV, E., & ALİ, A. J. (2021, January 1). Review Enhancement of Thermal Conductivity and Heat Transfer Using Carbon Nanotube for Nanofluids and Ionanofluids. Journal of Thermal Engineering, 7(1), 66–90. https://doi.org/10.18186/thermal.843077

[24] Erdem, O., & Demir, H. V. (2022). Oriented Self-Assembly of Colloidal Semiconductor Nanoplatelets on Liquid Interfaces. SpringerBriefs in Applied Sciences and Technology. https://doi.org/10.1007/978-981-19-7052-8

[25] Boles, M. A., Engel, M., & Talapin, D. v. (2016). Self-assembly of colloidal nanocrystals: From intricate structures to functional materials. In Chemical Reviews (Vol. 116, Issue 18, pp. 11220–11289). American Chemical Society. https://doi.org/10.1021/acs.chemrev.6b00196

[26] TUGOLUKOV, E., & ALİ, A. J. (2021, January 1). Review Enhancement of Thermal Conductivity and Heat Transfer Using Carbon Nanotube for Nanofluids and Ionanofluids. Journal of Thermal Engineering, 7(1), 66–90. https://doi.org/10.18186/thermal.843077

[27] Ambrosetti, A., Ferri, N., DiStasio, R. A., & Tkatchenko, A. (2016, March 11). Wavelike charge density fluctuations and van der Waals interactions at the nanoscale. Science, 351(6278), 1171–1176. https://doi.org/10.1126/science.aae0509

[28] Talapin, D. V., & Murray, C. B. (2005, October 7). PbSe Nanocrystal Solids for n- and p-Channel Thin Film Field-Effect Transistors. Science, 310(5745), 86–89. https://doi.org/10.1126/science.1116703

[29] Bigioni, T. P., Lin, X. M., Nguyen, T. T., Corwin, E. I., Witten, T. A., & Jaeger, H. M. (2006, March 19). Kinetically driven self assembly of highly ordered nanoparticle monolayers. Nature Materials, 5(4), 265–270. https://doi.org/10.1038/nmat1611

[30] Dong, A., Chen, J., Vora, P. M., Kikkawa, J. M., & Murray, C. B. (2010). Binary nanocrystal superlattice membranes self-assembled at the liquid-air interface. Nature, 466(7305), 474–477. https://doi.org/10.1038/nature09188

[31] de Oliveira, R., de Barros, A., & Ferreira, M. (2017). Nanostructured Films: Langmuir–Blodgett (LB) and Layer-by-Layer (LbL) Techniques. Nanostructures, 105–123. https://doi.org/10.1016/b978-0-323-49782-4.00004-8

[32] Aleksandrovic, V., Greshnykh, D., Randjelovic, I., Frömsdorf, A., Kornowski, A., Roth, S. V., Klinke, C., & Weller, H. (2008). Preparation and electrical properties of cobalt - Platinum nanoparticle monolayers deposited by the langmuir - Blodgett technique. ACS Nano, 2(6), 1123–1130. https://doi.org/10.1021/nn800147a

[33] Rupich, S. M.; Shevchenko, E. V.; Bodnarchuk, M. I.; Lee, B.; Talapin, D. V. Size-Dependent Multiple Twinning in Nanocrystal Superlattices. J. Am. Chem. Soc. 2010, 132 (1), 289−296. https://doi.org/10.1021/ja9074425

[34] Zhuang, J., Wu, H., Yang, Y., & Cao, Y. C. (2007, October 27). Supercrystalline Colloidal Particles from Artificial Atoms. Journal of the American Chemical Society, 129(46), 14166–14167. https://doi.org/10.1021/ja076494i

[35] Paik, T., Ko, D. K., Gordon, T. R., Doan-Nguyen, V., & Murray, C. B. (2011, September 21). Studies of Liquid Crystalline Self-Assembly of GdF3 Nanoplatelets by In-Plane, Out-of-Plane SAXS. ACS Nano, 5(10), 8322–8330. https://doi.org/10.1021/nn203049t

[36] Gao, Y., Weidman, M. C., & Tisdale, W. A. (2017, May 31). CdSe Nanoplatelet Films with Controlled Orientation of their Transition Dipole Moment. Nano Letters, 17(6), 3837–3843. https://doi.org/10.1021/acs.nanolett.7b01237

[37] Erdem, O., Gungor, K., Guzelturk, B., Tanriover, I., Sak, M., Olutas, M., Dede, D., Kelestemur, Y., & Demir, H. V. (2019, June 3). Orientation-Controlled Nonradiative Energy Transfer to Colloidal Nanoplatelets: Engineering Dipole Orientation Factor. Nano Letters, 19(7), 4297–4305. https://doi.org/10.1021/acs.nanolett.9b00681

[38] Momper, R., Zhang, H., Chen, S., Halim, H., Johannes, E., Yordanov, S., Braga, D., Blülle, B., Doblas, D., Kraus, T., Bonn, M., Wang, H. I., & Riedinger, A. (2020, March 12). Kinetic Control over Self-Assembly of Semiconductor Nanoplatelets. Nano Letters, 20(6), 4102–4110. https://doi.org/10.1021/acs.nanolett.9b05270

[39] Erdem, O., Foroutan, S., Gheshlaghi, N., Guzelturk, B., Altintas, Y., & Demir, H. V. (2020, July 31). Thickness-Tunable Self-Assembled Colloidal Nanoplatelet Films Enable Ultrathin Optical Gain Media. Nano Letters, 20(9), 6459–6465. https://doi.org/10.1021/acs.nanolett.0c02153

[40] Sun, X., & Geva, E. (2015, October 22). Equilibrium Fermi's Golden Rule Charge Transfer Rate Constants in the Condensed Phase: The Linearized Semiclassical Method vs. Classical Marcus Theory. The Journal of Physical Chemistry A, 120(19), 2976–2990. https://doi.org/10.1021/acs.jpca.5b08280

[41] Schuller, J. A., Karaveli, S., Schiros, T., He, K., Yang, S., Kymissis, I., Shan, J., & Zia, R. (2013, March 3). Orientation of luminescent excitons in layered nanomaterials. Nature Nanotechnology, 8(4), 271–276. https://doi.org/10.1038/nnano.2013.20

[42] Scott, R., Heckmann, J., Prudnikau, A. V., Antanovich, A., Mikhailov, A., Owschimikow, N., Artemyev, M., Climente, J. I., Woggon, U., Grosse, N. B., & Achtstein, A. W. (2017, September 18). Directed emission of CdSe nanoplatelets originating from strongly anisotropic 2D electronic structure. Nature Nanotechnology, 12(12), 1155–1160. https://doi.org/10.1038/nnano.2017.177

[43] Liu, Y., Li, N., Sun, R., Zheng, W., Liu, T., Li, H., Chen, Y., Liu, G., Zhao, H., Liu, H., & Zhang, Y. (2021, July). Stable metal-halide perovskites for luminescent solar concentrators of real-device integration. Nano Energy, 85, 105960. https://doi.org/10.1016/j.nanoen.2021.105960

[44] Chang, M. H., Das, D., Varde, P., & Pecht, M. (2012, May). Light emitting diodes reliability review. Microelectronics Reliability, 52(5), 762–782. https://doi.org/10.1016/j.microrel.2011.07.063

[45] Guzelturk, B., Kelestemur, Y., Olutas, M., Delikanli, S., & Demir, H. V. (2014, June 6). Amplified Spontaneous Emission and Lasing in Colloidal Nanoplatelets. ACS Nano, 8(7), 6599–6605. https://doi.org/10.1021/nn5022296

[46] Xiao, P., Huang, J., Yan, D., Luo, D., Yuan, J., Liu, B., & Liang, D. (2018, August 8). Emergence of Nanoplatelet Light-Emitting Diodes. Materials, 11(8), 1376. https://doi.org/10.3390/ma11081376

[47] Arkhipov, V. I., Emelianova, E. V., Tak, Y. H., & Bässler, H. (1998, July 15). Charge injection into light-emitting diodes: Theory and experiment. Journal of Applied Physics, 84(2), 848–856. https://doi.org/10.1063/1.368146

[48] van Dijken, A., Perro, A., Meulenkamp, E., & Brunner, K. (2003, September). The influence of a PEDOT:PSS layer on the efficiency of a polymer light-emitting diode. Organic Electronics, 4(2–3), 131–141. https://doi.org/10.1016/j.orgel.2003.08.007

[49] Haitao, X., & Xiang, Z. (2013, December 28). Investigation of hole injection enhancement by MoO3 buffer layer in organic light emitting diodes. Journal of Applied Physics, 114(24). https://doi.org/10.1063/1.4852835

[50] Hou, L., Liu, P., Li, Y., & Wu, C. (2009, July). Enhanced performance in organic light-emitting diodes by sputtering TiO2 ultra-thin film as the hole buffer layer. Thin Solid Films, 517(17), 4926–4929. https://doi.org/10.1016/j.tsf.2009.03.017

[51] Shibata, M., Sakai, Y., & Yokoyama, D. (2015). Advantages and disadvantages of vacuum-deposited and spin-coated amorphous organic semiconductor films for organic light-emitting diodes. Journal of Materials Chemistry C, 3(42), 11178–11191. https://doi.org/10.1039/c5tc01911g

[52] Yu, J. C., Lee, A. Y., Kim, D. B., Jung, E. D., Kim, D. W., & Song, M. H. (2017, April 24). Enhancing the Performance and Stability of Perovskite Nanocrystal Light-Emitting Diodes with a Polymer Matrix. Advanced Materials Technologies, 2(6), 1700003. https://doi.org/10.1002/admt.201700003

[53] Wu, J., Wei, M., Fu, Y., & Cui, C. (2021, April 6). Color mismatch and observer metamerism between conventional liquid crystal displays and organic light emitting diode displays. Optics Express, 29(8), 12292. https://doi.org/10.1364/oe.418675

[54] Agudo, J., Pardo, P., Sánchez, H., Pérez, N., & Suero, M. (2014, July 7). A Low-Cost Real Color Picker Based on Arduino. Sensors, 14(7), 11943–11956. https://doi.org/10.3390/s140711943

[55] Woo, S. J., Kim, J. S., & Lee, T. W. (2021, August 27). Characterization of stability and challenges to improve lifetime in perovskite LEDs. Nature Photonics, 15(9), 630–634. https://doi.org/10.1038/s41566-021-00863-2

[56] Altintas, Y., Liu, B., Hernández-Martínez, P. L., Gheshlaghi, N., Shabani, F., Sharma, M., Wang, L., Sun, H., Mutlugun, E., & Demir, H. V. (2020, August 25). Spectrally Wide-Range-Tunable, Efficient, and Bright Colloidal Light-Emitting Diodes of Quasi-2D Nanoplatelets Enabled by Engineered Alloyed Heterostructures. Chemistry of Materials, 32(18), 7874–7883. https://doi.org/10.1021/acs.chemmater.0c02630

[57] Altintas, Y., Gungor, K., Gao, Y., Sak, M., Quliyeva, U., Bappi, G., Mutlugun, E., Sargent, E. H., & Demir, H. V. (2019, August 22). Giant Alloyed Hot Injection Shells Enable Ultralow Optical Gain Threshold in Colloidal Quantum Wells. ACS Nano, 13(9), 10662–10670. https://doi.org/10.1021/acsnano.9b04967

[58] Qian, L., Zheng, Y., Xue, J., & Holloway, P. H. (2011, August 7). Stable and efficient quantum-dot light-emitting diodes based on solution-processed multilayer structures. Nature Photonics, 5(9), 543–548. https://doi.org/10.1038/nphoton.2011.171

[59] Alexandrov, A., Zvaigzne, M., Lypenko, D., Nabiev, I., & Samokhvalov, P. (2020, May 4). Al-, Ga-, Mg-, or Li-doped zinc oxide nanoparticles as electron transport layers for quantum dot light-emitting diodes. Scientific Reports, 10(1). https://doi.org/10.1038/s41598-020-64263-2

[60] Chutinan, A., Ishihara, K., Asano, T., Fujita, M., & Noda, S. (2005, February). Theoretical analysis on light-extraction efficiency of organic light-emitting diodes using FDTD and mode-expansion methods. Organic Electronics, 6(1), 3–9. https://doi.org/10.1016/j.orgel.2004.12.001

[61] Baruj, H. D., Bozkaya, I., Canimkurbey, B., Isik, A. T., Shabani, F., Delikanli, S., Shendre, S., Erdem, O., Isik, F., & Demir, H. V. (2023, April 6). Highly-Directional, Highly-Efficient Solution-Processed Light-Emitting Diodes of All-Face-Down Oriented Colloidal Quantum Well Self-Assembly. Small, 19(29). https://doi.org/10.1002/smll.202206582

[62] Jiawen Liu. Fluorescence Properties of Colloidal Semiconducting Nanoplatelets: from Single Emitters to Self-Assemblies. Optics [physics.optics]. Sorbonne Université, 2020. English. NNT: 2020SORUS218. tel-03414015v2ff